Microscale Thermophoresis Analysis of Membrane Proteins

Nawaz Nighat, Ali Roshan, Ali Muhammad, Manfield Iain W., Taj Muhammad Kamran, Mustafa Mohammad Zahid, Simon G Patching

Review article

Microscale Thermophoresis Analysis of Membrane Proteins

Nighat Nawaz[1,2], Roshan Ali[3], Muhammad Ali[3], Iain W. Manfield[4], Muhammad Kamran Taj[5], Mohammad Zahid Mustafa[5] and Simon G. Patching[1,*]

[1]School of Biomedical Sciences (Astbury Building), University of Leeds, Leeds LS2 9JT, UK
[2]Department of Chemistry, Islamia College Peshawar, Peshawar 25120, Pakistan
[3]Institute of Basic Medical Sciences, Khyber Medical University, Peshawar 25100, Pakistan
[4]School of Molecular and Cellular Biology, University of Leeds, Leeds LS2 9JT, UK
[5]Centre for Advanced Studies in Vaccinology and Biotechnology, University of Balochistan, Quetta 08763, Pakistan

*Correspondence: Professor Simon G. Patching
E-mail: s.g.patching@leeds.ac.uk, simonpatching@yahoo.co.uk

Abstract
Microscale thermophoresis (MST) is an analytical technique for measuring biomolecular interactions. It is based on the physical phenomenon that particles move within temperature gradients, which is affected by their size, charge, hydration shell and conformation. The MST sample must contain a fluorescent target molecule used to observe the movement of particles, and this can be titrated with an unlabelled binding partner for quantifying the interaction. MST is highly sensitive, using relatively small amounts of sample, and it has no limitations on the size of the target biomolecule, on the affinity of the interaction or on the composition of the buffer and other sample components. This makes MST ideally suited to characterising interactions with membrane proteins, which can be studied in cell lysates, native membranes, solubilised in detergents or reconstituted in lipids. The intrinsic aromatic residues of membrane proteins have been used as the fluorophore for MST (label-free MST) or membrane proteins have been labelled with a range of fluorescent dyes or conjugated with fluorescent proteins (labelled MST). The different types of membrane proteins that have had biomolecular interactions characterised by MST include the SARS-CoV-2 spike protein, GPCRs and other receptors, sensor kinases, ion channels, aquaporins, and transport proteins.

Key words: Biomolecular interactions, fluorescent labelling, ligand binding, drug screening, SARS-CoV-2 spike protein, GPCRs, receptors, ion channels, aquaporins, transport proteins

---

1. Introduction

Microscale thermophoresis (MST) is a biophysical technique for measuring biomolecular interactions. It is based on the physical phenomenon that particles move within temperature gradients, usually from regions of higher to lower temperature. The movement of particles is affected by their size, charge, hydration shell and conformation, any of which can change during biomolecular interactions [1-10]. In MST a microscopic temperature gradient is induced by infrared laser light and the sample must contain a fluorescent target molecule that is used to observe the movement of particles. The fluorescent molecule is kept at a constant concentration and is titrated with a range of concentrations of an unlabelled binding partner. The movement of fluorescent molecules within the temperature gradient results in a quantifiable change in their local concentration and therefore of the measured fluorescence, thus enabling estimation of binding affinities. The necessary fluorescence property may be intrinsic to one of the binding partners (e.g., from aromatic residues in a protein) (label-free MST) or a fluorescent dye or other fluorescent protein (e.g., green fluorescent protein, GFP) must be attached to one of the binding partners (labelled MST). MST can measure many types of

OSF Preprint 2024 DOI: 10.31219/osf.io/pe7ut

biomolecular interactions, including protein-protein, protein-nucleic acid, protein-lipid, protein-small molecule/peptide/ion or protein-liposome/vesicle interactions. It can also measure conformation changes in a biomolecule that is subjected to varying conditions. In addition to binding affinities, MST can be used to assess other physical parameters of biomolecules and their interactions such as aggregation and precipitation, stoichiometry and oligomerisation.

2. The MST experiment

In the MST instrument (Figure 1A), samples are measured in fine glass capillaries with a typical total volume of 4 µl. The capillary contains a solution of a fluorescent target molecule and a binding partner. The fluorescent molecule is excited using an appropriate wavelength of light and the emitted fluorescence is detected, both through the same objective lens. An infrared laser is focussed into the capillary to create a microscopic temperature gradient at the exact spot where fluorescence emission is detected. This gradient is focused on a diameter of around 50 µm and typically contains a temperature difference of 2-6 °C.

The MST experiment (Figure 1B) begins with the IR laser switched off, where molecules are homogenously distributed and diffuse freely within the sample. At this point the initial fluorescence intensity is detected. When the IR laser is switched on there is immediate heating of the focussed area resulting in a rapid change in fluorophore properties and a strong decrease in fluorescence intensity before thermophoresis begins. This is followed by thermophoretic movement of the fluorescent molecules out of the heated area resulting in a slow decrease in fluorescence intensity. A steady state is typically reached after around 30 seconds. The IR laser is then turned off resulting in an immediate increase in fluorescence intensity. As the sample cools down there is movement of fluorescent molecules back into the area that was heated to give further increase is fluorescence intensity. For each sample, the normalised fluorescence (F_{norm}) is calculated from the initial fluorescence (F_0) and from the fluorescence after thermophoresis (F_1), as follows: $F_{norm} = F_1/F_0$. The change in the normalised fluorescence against the change in concentration of binding partner can be used to quantify the affinity of the binding interaction.

3. Advantages of MST

MST is a relatively simple, robust, and rapid technique that has several advantages over other biophysical techniques commonly used to measure biomolecular interactions such as surface plasmon resonance (SPR), isothermal titration calorimetry (ITC), dynamic light scattering (DLS), fluorescence spectroscopy, nuclear magnetic resonance (NMR) spectroscopy, and mass spectrometry (MS) [6, 9, 11-20]. MST has no limitations on the size of the target biomolecule or on the affinity of the interaction to be measured (pM to mM) or on the composition of the buffer and other sample components. The sample may contain detergents or lipids and MST measurements can be performed on complex samples such as cell lysates or membrane preparations. Unlike in SPR, the target biomolecule does not need to be immobilised. MST is highly sensitive, so a principal advantage is that experiments use relatively small amounts of sample. For example, a full titration using sixteen capillaries each containing 4 µl and performed in triplicate would use a total volume of 192 µl. This would contain a total of 1.92-19.20 picomoles of fluorescent biomolecule if at a concentration of 10-100 nM. It follows that assay optimisation also has low sample consumption. MST measurements in the instrument are relatively quick, taking around 40 seconds per sample/titration point, so a full titration with a series of 16 dilutions can be run in under 15 minutes. These advantages mean that MST is particularly well suited to studying membrane proteins that are often large and must be kept in a membrane, lipid or detergent environment to retain their native structure and activity, and some, especially eukaryotic proteins, can only be obtained in small quantities.

4. MST analysis of membrane proteins

When manipulating a membrane protein with a fluorophore for MST measurements, any potential effects of the fluorophore on the native structure and activity of the protein should be considered and tested for. This should include the use of appropriate controls in the MST measurements and may require the use of other biophysical and biochemical analyses to test structural integrity and activity. Such effects can be avoided if native aromatic residues in a target membrane protein can be used as the fluorophore for MST measurements, but only four of the studies on membrane proteins (4/60) employed this approach (Table S1). On the face of it use of native aromatic residues is more straightforward than reacting the target membrane protein with a fluorescent dye or conjugating it with a fluorescent protein, but the intensity of intrinsic fluorescence produced in most membrane proteins studied was presumably not high enough for efficient detection.

OSF Preprint 2024 DOI: 10.31219/osf.io/pe7ut

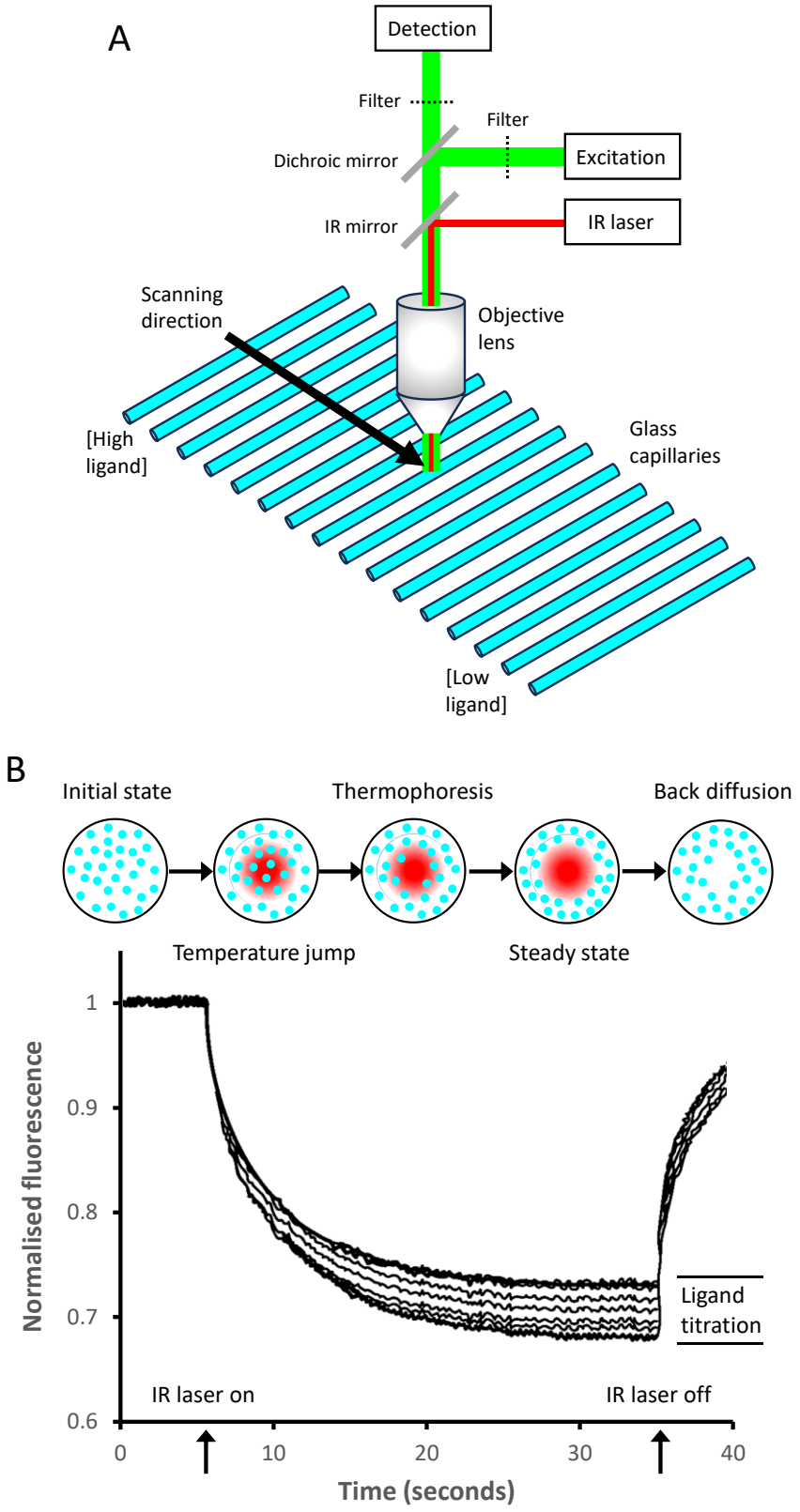

Figure 1. The MST experiment. In the MST instrument (**A**) a series of sixteen glass capillaries (volume 4 µl) are filled with samples containing a constant concentration of a fluorescent target biomolecule and a range of concentrations of a binding partner (e.g. a ligand). The samples are scanned in turn by being subjected to heating at a microscopic area (50 µm diameter) using an IR laser, which creates a temperature gradient. Fluorescence is measured at the same area to follow movement of the target biomolecules. In the profile of the MST experiment (**B**) the initial fluorescence is measured then the IR laser is turned on (5 seconds). This induces an immediate temperature jump and then movement of the target biomolecule away from the heated area (thermophoresis) takes place until a steady state is reached (~30 seconds). The IR laser is turned off (35 seconds) then there is back diffusion of the target biomolecule. The magnitude of the thermophoresis, and therefore the normalised fluorescence intensity, are altered by different concentrations of the ligand.

OSF Preprint 2024 DOI: 10.31219/osf.io/pe7ut

One strategy that avoids manipulating the target membrane protein with a fluorophore is to reconstitute it in nanodiscs that have themselves been reacted with a fluorescent dye. For example, MST measurements were performed on the human neurotensin receptor NTS1 reconstituted in nanodiscs formed using fluorescently labelled membrane scaffold protein MSP1D1. MST measured binding of the G-protein subunit Gαi1 to NTS1 in Alexa Fluor™ 647-labelled MSP1D1 nanodiscs formed using different lipids and in the presence of different NTS1 ligands. The affinity of Gαi1 binding to NTS1 was influenced by the lipid composition of the nanodiscs, where the highest affinities were obtained using porcine brain polar lipid (BPL) in the absence of ligand (K_D = 300 ± 100 nM) and in the presence of agonist neurotensin (K_D = 140 ± 60 nM). Empty nanodiscs (no NTS1) did have a similar binding affinity in the presence of neurotensin (K_D = 200 ± 100 nM). For comparison, affinities in the presence of antagonists SR48692 or SR142948A were 600 ± 300 nM and 300 ± 100 nM, respectively, and in the presence of a non-hydrolysable analogue of GTP (GTPγS) (negative control) the affinity was 1.5 ± 0.8 μM [21].

5. Fluorophores used in MST measurements on membrane proteins

Out of the 60 different studies that have used MST to analyse membrane proteins (Table S1) over a half (52.5%) have employed commercial kits designed to be used with Monolith MST instruments. The majority of these kits were red (17/60) or blue (4/60) dyes containing a succinimidyl ester group that reacts with the primary amines on lysine residues to form a covalent bond. Some the of kits (8/60) were red dyes that react with His-tags engineered on to the target biomolecule, which can be used with either purified proteins or crude samples (e.g. cell lysates). A few of the kits (2/60) were green dyes containing a maleimide reactive fluorophore that reacts with cysteine residues to form a covalent bond. All of these kits are generally optimised for proteins with a molecular weight of more than 5 kDa and concentrations of 2-20 μM. The next most common type of fluorophore used with membrane proteins were three Alexa Fluor™ dyes (488, 546, 647) (7/60) (Figure 2).

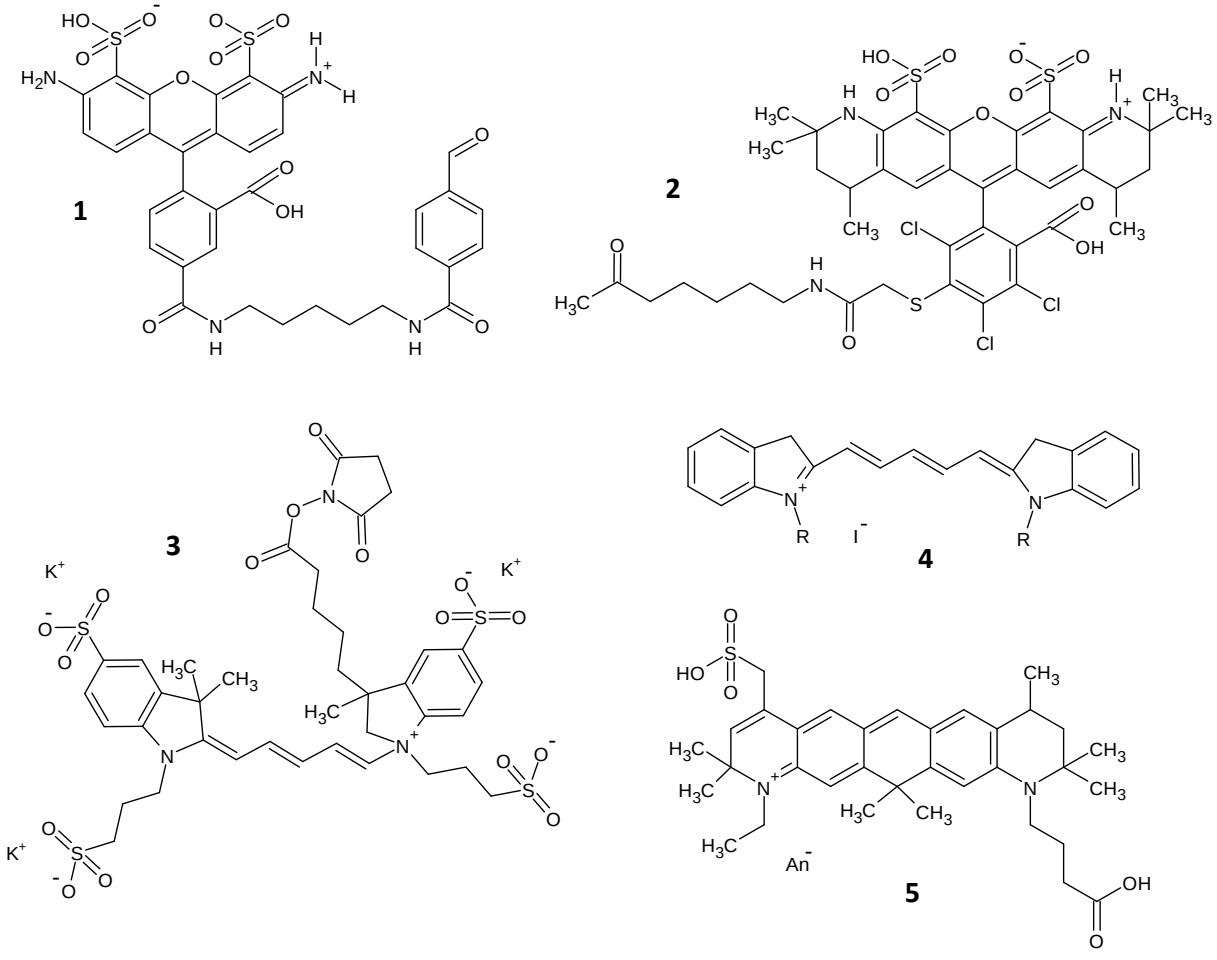

Figure 2. Chemical structures of some fluorophores used in MST measurements on membrane proteins. Alexa Fluor™ 488 (**1**), Alexa Fluor™ 546 (**2**), Alexa Fluor™ 647 (**3**) Cy5 (**4**), Atto-647 (**5**).

OSF Preprint 2024 DOI: 10.31219/osf.io/pe7ut

Alexa Fluor™ 488 (**1**) is a bright green dye with excitation suited to the 488 nm laser line. Alexa Fluor™ 546 (**2**) is a bright orange dye that can be excited using 488 nm or 532 nm laser lines. Alexa Fluor™ 647 (**3**) is a bright far-red dye with excitation suited to the 633 nm laser line, it contains a succinimidyl ester group that can react with the primary amines of lysine residues. In some studies (4/60) the target membrane protein was conjugated to GFP, which can be excited by the 488 nm laser line. GFP from *Aequorea victoria* (water jellyfish) is comprised of 238 amino acids (26.9 kDa) (UniProt P42212) and has a β-barrel structure with eleven β-strands [22, 23]. The chromophore of GFP consists of the three amino acids Ser-dehydroTyr-Gly) (residues 65-67), which have been mutated (F64LT) to create enhanced GFP (eGFP) that has increased fluorescence intensity, greater photostability and higher efficiency compared to wild-type [24, 25]. Three of the studies (3/60) used the dye Cy5 (1,1′-dimethyl-3,3,3′,3′-tetramethylindocarbocyanine) (**4**) as fluorophore (Figure 2), which is a far-red fluorescent dye with excitation suited to the 633 nm or 647 nm laser lines. Cy5 contains an amine group that can be reacted with activated esters and other electrophilic reagents. One study (1/60) used the zwitterionic red dye Atto-647 (**5**) as fluorophore (Figure 2), for which suitable excitation sources are next to the He:Ne laser (633 nm), the 647 nm line of the Krypton-Ion laser or a diode-laser emitting at 650 nm.

6. Membrane proteins analysed by MST

The different types of membrane proteins that have had biomolecular interactions characterised by MST include the severe acute respiratory syndrome coronavirus 2 (SARS-CoV-2) spike protein, GPCRs and other receptors, sensor kinases, ion channels, aquaporins, transport proteins, and others.

6.1. SARS-CoV-2 spike protein

In recent years eleven studies have employed MST to analyse various interactions with the SARS-CoV-2 spike protein, which binds to the angiotensin-converting enzyme 2 (ACE2) receptor on target human cells. MST was used to measure the binding of bacterial (*Escherichia coli*) lipopolysaccharide to the full-length (residues 16 to 1213) fluorescently-labelled SARS-CoV-2 spike protein, giving a K_D of 46.7 ± 19.7 nM [26]. Various techniques were used to investigate the molecular mechanism of how the SARS-CoV-2 spike protein augments lipopolysaccharide-mediated hyperinflammation, where the spike protein serves as a lipopolysaccharide delivery system to its receptors. This included use of MST to measure the binding affinity of lipopolysaccharide to the SARS-CoV-2 spike protein Wuhan variant (K_D = 46.7 ± 19.7 nM) and Omicron variant (K_D = 3.3 ± 1.5 μM), of lipopolysaccharide to Wuhan S1 (K_D = 50.0 ± 20.0 nM) and Omicron S1 (K_D = 4.6 ± 1.7 μM), and of lipid A to subunit Wuhan S1 (42.2 ± 24.4 nM) and Omicron S1 (K_D = 0.6 ± 0.2 μM). Binding of lipopolysaccharide to Wuhan S2 (K_D = 3.6 ± 1.6 μM) had a weaker affinity than for S1 [27].

In a study that used machine learning models to identify inhibitors of SARS-CoV-2 through the repurposing of existing drugs, MST was used to measure binding of the antimalarial drug lumefantrine to the SARS-CoV-2 spike protein receptor binding domain (RBD). Residues 331 to 528 of the spike protein were expressed and purified and labelled with the amine reactive dye RED-NHS. Titration of lumefantrine with the spike protein RBD produced a K_D of 259 ± 78 nM [28]. MST measured binding of the fungal defensin micasin from *Microsporum canis* to the spike protein RBD. The latter was labelled with the fluorescent dye NT−495−NHS and in MST experiments titrated with wild-type micasin and some mutant forms. Micasin bound to the spike protein RBD with a K_D of 5.04 ± 0.96 μM [29]. A study used various computational and experimental approaches to identify molecules that could be optimised to improve anti-SARS-CoV-2 activity. Five beta-blockers (pindolol, carvedilol, carteolol, atenolol, and bisoprolol) against the SARS-CoV-2 spike protein RBD were identified. The highest affinity of these was carvedilol, for which MST measured a K_D value of 364 ± 22 nM [30]. In a study that designed high-affinity affibody ligands for purification of the RBD from coronavirus spike proteins, MST was used to measure binding of ZRBD-02 (K_D = 133.4 nM), ZRBD-04 (K_D = 377.3 nM), and ZRBD-07 (K_D = 36.3 nM) to the SARS-CoV-2 spike protein RBD [31].

One of the studies designed and tested six synthetic ACE2-based peptides to antagonise the interaction between ACE2 and the spike protein RBD based on molecular docking with crystal structures of their interface. The ability of the peptides to inhibit the ACE2-spike-RBD interaction was tested using a luciferase assay, then the affinity of peptide binding to the spike-RBD protein was measured by MST. The purified spike-RBD protein was fluorescently labelled and incubated with each peptide at a range of concentrations (12.5–0.00019 μM). Some of the peptides had binding affinities in the low nanomolar range, with the highest affinity peptides having K_D values of 13 and 45 nM [32]. In a different study synthetic α-helical peptides mimicking the α1-helix motif of the ACE2 receptor were tested as potential inhibitors of the ACE2 SARS-CoV-2 interaction. A series of peptides N-capped with either Ac-βHAsp-[ProM-5] or Ac-βHAsp-PP were tested and MST measurements demonstrated a strong binding affinity (K_D = 62 nM) of an Ac-βHAsp-PP-

OSF Preprint 2024 DOI: 10.31219/osf.io/pe7ut

capped peptide for the SARS-CoV-2 spike protein RBD [33]. MST was used to confirm how C-2 thiophenyl tryptophan trimers inhibit cellular entry of SARS-CoV-2 through interaction with the spike protein. MST measured binding of compounds to the spike protein and to its RBD, and also the effect of the compounds on interaction of the spike protein and its RBD with ACE2 [34]. Following a study to measure differential interactions between human ACE2 and the spike RBD of SARS-CoV-2 variants of concern [35], a later study used a combination of steered molecular dynamics (SMD) simulation and experimental MST to quantify the interaction between the Omicron variant of the RBD and human ACE2 [36]. MST measurements of binding between human ACE2 and different mutants of the RBD were directed by the SMD simulation. It was identified that Omicron produces an enhanced RBD-ACE2 interaction through mutations N501Y, Q498R and T478K in the RBD. The Omicron variant of the RBD had a five-fold higher affinity for ACE2 (K_D = 5.5 ± 1.4 nM) than did the wild-type RBD (K_D = 27.5 ± 4.8 nM), and higher affinities than the RBDs of the Alpha (K_D = 11.8 ± 0.8 nM), Beta (K_D = 23.1 ± 2.4 nM) and Delta (K_D = 21.5 ± 2.9 nM) variants [36].

6.2. G protein-coupled receptors

Nine studies have employed MST to analyse binding interactions to different GPCRs. In a study that reported structure and function analyses of the purified GPCR human vomeronasal type 1 receptor 1, MST using native tryptophan residues as the fluorophore showed binding of hVN1R1 to its ligand myrtenal, giving an EC_{50} of approximately 1 μM [37]. In three similar studies, MST was used to measure binding of human and mouse olfactory receptors and GPCRs solubilised with designer lipid-like peptides to their respective ligands. Here native tryptophan residues in the receptors were used as the fluorescence source for MST, and measured EC_{50} values ranged from 0.9 to 86 μM [38-40]. In a study reporting the cell-free expression, purification and ligand-binding analysis of olfactory receptors DmOR67a, DmOR85b and DmORCO from *Drosophila melanogaster*, MST was used to demonstrate that they bind their respective ligands. DmOR67a and DmORCO were titrated individually and together with ethyl benzoate, while DmOR85b and DmORCO were titrated individually and together with 2-heptanone. When DmOR67a was co-incubated with DmORCO, ethyl benzoate bound with an affinity of ~0.5 ± 0.1 μM, and when DmOR85b was co-incubated with DmORCO, 2-heptanone bound with an affinity of ~0.8 ± 0.2 μM [41].

In a study that computationally designed and characterised nanobody-derived peptides (NDPs) to stabilise the active conformation of the human β2-adrenergic receptor (β2-AR), MST measured binding of a selected 17-residue NDP (P3) to the β2-AR. The agonist(isoproterenol)-activated β2-AR displayed a ~10-fold higher affinity for P3 than the unstimulated receptor, with EC_{50} values of 3.57 μM and 58.22 μM, respectively [42]. MST was used to observe binding of the peptide neurotransmitter neurotensin (NT) to the human dopamine receptor 1 (D1) under native conditions in polymer-assembled Lipodisqs (Figure 3).

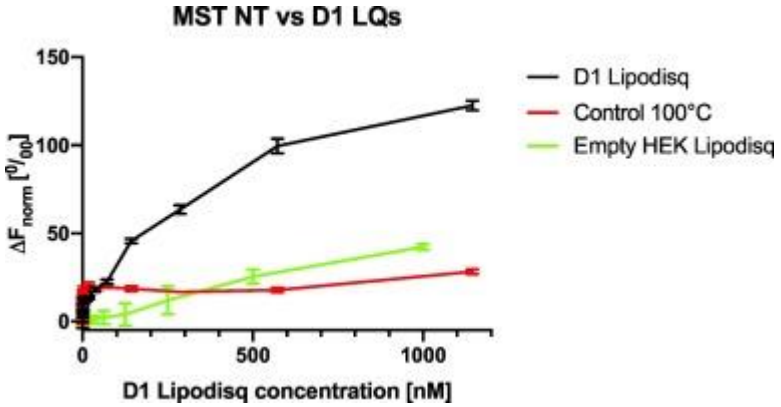

Figure 3. Binding of neurotensin (NT) to the human dopamine receptor 1 (D1) in polymer-assembled Lipodisqs. MST used Cy5-labelled NT (NT-Cy5). The affinity of NT-Cy5 for D1 Lipodisqs was >300 nM. Denatured D1 Lipodisqs and Lipodisqs formed from HEK cells lacking D1 (red and green curves, respectively) did not show binding to NT. Error bars represent the standard error of n = 3 measurements. This figure was reproduced from Bada Juarez et al. (2020) [43].

The Lipodisqs were formed by adding the copolymer styrene-maleic acid (SMA) to membranes expressing D1 at a membrane:SMA w/w ratio of 1:1.5. MST measurements used Cy5-labelled NT, which had an estimated binding affinity for D1 Lipodisqs of >300 nM [43]. An MST method was developed to measure ligand/receptor binding in non-purified samples of the dopamine D2 receptor (D2R). The concentration of D2R in mammalian cell plasma membranes from induced HekD2 cells was determined to be 36.8 ± 2.6

OSF Preprint 2024 DOI: 10.31219/osf.io/pe7ut

pmol/mg. Dose-response curves determined the binding affinity (K_D) for the fluorescent ligand spiperone—Cy5 to be 5.3 ± 1.7 nM. To eliminate the possibility of non-specific binding between spiperone—Cy5 and the cell membranes, the measurements were performed both in the absence and in the presence of the D2R antagonist haloperidol [44].

In a study demonstrating that down-regulation of the endothelial protein C receptor (EPCR) promotes preeclampsia by affecting actin polymerization, MST was used to observe direct binding of EPCR to protease-activated receptor 1 (PAR-1), which is a GPCR [45]. A plethora of techniques were used to identify macrophage migration inhibitory factor (MIF) as an atypical chemokine (ACK) that binds to chemokine receptors CXCR2 and CXCR4 to promote atherogenic leukocyte recruitment. This included use of MST to confirm the interaction between MST-Red-labelled MIF and platelet chemokine CXCL4L1. Titration of MST-Red-MIF with increasing concentrations of CXCL4L1 produced a binding constant (K_D = 159.8 ± 16.8 nM) that was similar to that obtained by SPR (K_D = 116 ± 16 nM) [46].

6.3. Other receptors

Various other receptors have been analysed by MST, including measurement of metallothionein binding to the lipocalin-2 (24p3/neutrophil gelatinase-associated lipocalin (NGAL)) receptor (SLC22A17) in CHO plasma membrane vesicles, giving an EC_{50} of 123 ± 50 nM [47]. MST was used to characterise interactions between the membrane-bound mucin MUC4 and the ErbB2 receptor, which occurs at the cancer cell surface. Lysates of CHO cells were used that contained the transmembrane β subunit of MUC4 (MUC4β) or a mutant containing only the EGF domains (MUC4EGF3+1+2). K_D values for binding of ErbB2 to MUC4β-ErbB2 and MUC4EGF3+1+2 were measured at 7-25 nM and 65-79 nM, respectively [48].

MST was used to analyse ligand-specific conformational states of the human glycine receptor (GlyR), which is a member of the pentameric ligand-gated ion channel (pLGIC) family. The fluorescent-labelled GlyR alpha-1 subunit was solubilised in amphipathic styrene-maleic acid copolymer nanodiscs. MST measurements showed that the full agonist glycine and the partial agonist taurine induced different conformational transitions on binding to the GlyR, giving EC_{50} values of 65 ± 22.8 μM and 473.8 ± 66.1 μM, respectively (Figure 4). The results indicated that partial agonism in pLGIC proteins is reflected by the adaption of distinct receptor conformations [49].

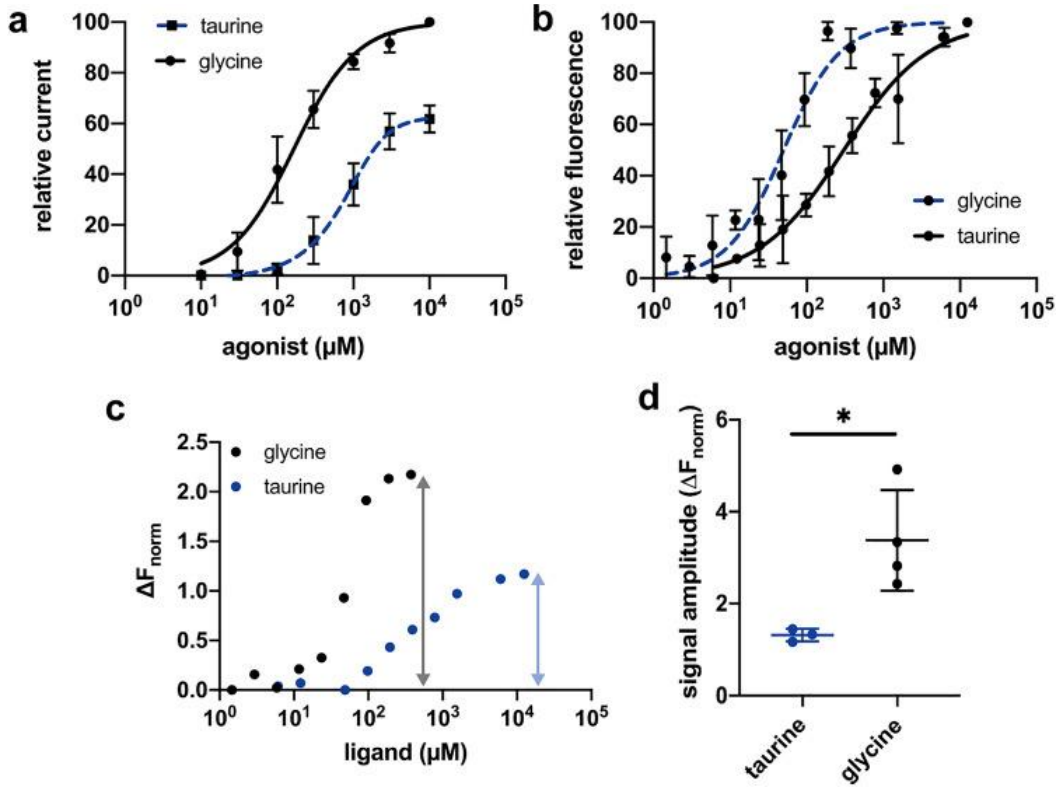

Figure 4. Legend on following page.

OSF Preprint 2024 DOI: 10.31219/osf.io/pe7ut

Figure 4. Binding characteristics of the partial agonist taurine to α1-GFP GlyR nanodiscs. (a) Dose–response data for glycine and taurine of heterologous expressed α1 GlyR from *Xenopus laevis* oocytes. Taurine acts as a partial agonist with an a EC_{50} value of 843 ± 16 μM reaching a maximum current of 61% compared to glycine (n = 3). Taurine currents are normalized to the maximum glycine currents for each cell. Error bars represent SEM. (b) MST binding experiment of α1-GFP GlyR with a taurine titration series of 6 μM to 12.5 mM results in a cEC_{50} value of 473.8 ± 46.1 μM (n = 3). Error bars represent SEM. (c) Exemplary α1-GFP GlyR MST data of taurine (blue circles) and glycine (black circles) obtained from oocytes displaying a difference in their maximal thermophoretic mobility (grey and blue arrows). (d) Comparison of the signal amplitudes of α1-GFP GlyR SMALPs expressed in HEK293 cells and oocytes for glycine and taurine. Binding of taurine leads to a significant decreased thermophoretic movement (p = 0.024, unpaired two-side t test, n = 3) with signal amplitudes of 1.32 ± 0.14 compared to glycine-bound receptors with signal amplitudes of 3.38 ± 1.09. Data are shown in mean ± SD. This figure was reproduced from Bernhard and Laube (2020) [49].

MST was used to measure binding of FIP-nha (a fungal immunomodulatory protein from *Nectria haematococca*) to the labelled human epidermal growth factor receptor EGFR (K_D = 15.54 ± 2.93 μM) [50]. In a study that performed in silico screening of the binding affinities of fifty curcumin derivatives to the human EGFR by a molecular docking approach, MST was used to validate the results. The predicted EGFR-ligand binding constants were in the range of 0.00013 ± 0.00006 to 3.45 ± 0.10 μM. MST measured binding constants for curcumin (K_D = 5.1 ± 0.33 μM), N-(3-nitrophenylpyrazole) curcumin (K_D = 19.7 ± 2.1 μM), and derivative 1A9 (K_D = 4.9 ± 0.62 μM) [51].

A study demonstrated how the chemotherapeutic agent cisplatin interacts with toll-like receptor 4 (TLR4) to initiate proinflammatory signalling that underlies cisplatin toxicities. Soluble TLR4 blocked cisplatin-induced, but not lipopolysaccharide-induced, TLR4 activation. In MST experiments nickel and cisplatin, but not lipopolysaccharide, showed direct binding to human TLR4 with K_D values of 2.72 μM and 50.57 μM, respectively. Mouse TLR4 showed binding to cisplatin (K_D = 104.9 μM) but not to nickel [52].

MST was used to measure binding of lipoprotein ligands to two human class B scavenger receptors, scavenger receptor class B type 1 (SR-B1) and CD36, which are receptors for high-density lipoproteins and oxidized low-density lipoproteins, respectively. Using receptors labelled with Cy5 at lysine residues, SR-B1 bound to lipid-free apolipoprotein A-I with a K_D of 82 ± 12 μg/ml or 2.73 ± 0.40 μM and to holoparticle high-density lipoprotein (HDL) with a K_D of 52 ± 9 μg/ml or 194 ± 34 nM. CD36 bound oxidized low-density lipoprotein (oxLDL) with a K_D of 1.2 ± 0.5 mg/ml or 342.86 ± 285.71 nM and bound human HDL with a K_D of 33 ± 8 μg/ml or 123.36 ± 29.9 nM. There was no difference in affinity of SR-B1 for HDL or CD36 for oxLDL when comparing glycosylated and deglycosylated receptors [53].

MST was also used to measure binding of Staphylococcus enterotoxin B (SEB) to the human natural killer cell receptor 2B4 (CD244) [54].

6.4. Sensor kinases

MST has been used to analyse some histidine and tyrosine kinases. In a study that investigated interactions in the Cpx two component system of *Escherichia coli*, MST was used to measure binding affinities between the sensor histidine kinase CpxA with its cognate response regulator CpxR and its accessory protein CpxP. CpxA was reconstituted in MSP1D1 nanodiscs and MST measurements used fluorescently-labelled CpxA-Strep or MSP1D1. CpxA had a high affinity for CpxR (K_D = 3.7 ± 0.5 μM), which was increased by around 10-fold by phosphorylation (K_D = 0.55 ± 0.06 μM). The affinity between CpxA and CpxP was much lower (K_D >100 μM) [55].

A range of biophysical techniques and cell-based assays were used to identify a highly selective small molecule inhibitor of lemur tyrosine kinase 3 (LMTK3), which is a dual specificity serine/threonine kinase with an oncogenic role in various tumour types and a viable therapeutic target. The analyses included use of MST to obtain binding curves for the new inhibitor C36 (K_D = 1.87 ± 0.2 μM) and an existing inhibitor C28 (K_D = 2.50 ± 0.4 μM) with human LMTK3 [56].

6.5. Ion channels

Several studies have used MST to analyse interactions with the voltage-dependent anion channel 1 (VDAC1). In a study that looked at mediation of the antiapoptotic activity of Bcl-xL protein upon interaction with mouse VDAC1, MST was used to observe binding of fluorescently labelled Bcl-xL to VDAC1, giving a binding affinity of 0.67 μM [57]. In a study that demonstrated direct modulation of human VDAC1 by cannabidiol (CBD), MST was used to show a direct interaction between purified fluorescently labelled VDAC1 and CBD, giving a K_D of 11.2 ± 6 μM [58]. In a study that demonstrated how VDAC1 mediates amyloid β (Aβ) toxicity and is a potential target for Alzheimer's disease therapy, MST was used to observe

OSF Preprint 2024 DOI: 10.31219/osf.io/pe7ut

Aβ binding to fluorescently-labelled human VDAC1 with a K_D of 50 μm. In an MST experiment using intrinsic VDAC1 tryptophan fluorescence, Aβ binding resulted in a K_D of 16.6 μM [59]. Seventeen small-molecule compounds were screened for interaction with human mitochondrial VDAC1 using nano-differential scanning fluorimetry and MST (Figure 5). The dissociation constants for fifteen of the compounds were measured by MST with six successfully determined: DIDS (K_D = 0.5 μM), VBIT4 (K_D = 3 μM), itraconazole (K_D = 5 μM), cannabidiol (K_D = 6 μM), curcumin (K_D = 6 μM), emodin (K_D = 10 μM). It was noted that DIDS is likely to interact covalently with VDAC1, which should be considered in evaluating the measured K_D. Four of the compounds (cannabidiol, curcumin, DIDS and VBIT4) were identified as potential starting points for future design of VDAC1 selective ligands [60]. In a study that demonstrated how a cholesterol analogue induces an oligomeric reorganization of VDAC, MST was used to measure binding of hexokinase isoform I (HK-I) to VDAC from *Neurospora crassa*, giving a binding constant of 27 ± 6 μM in the presence of cholesteryl-hemisuccinate. There was no binding of hexokinase isoform II (HK-II) [61].

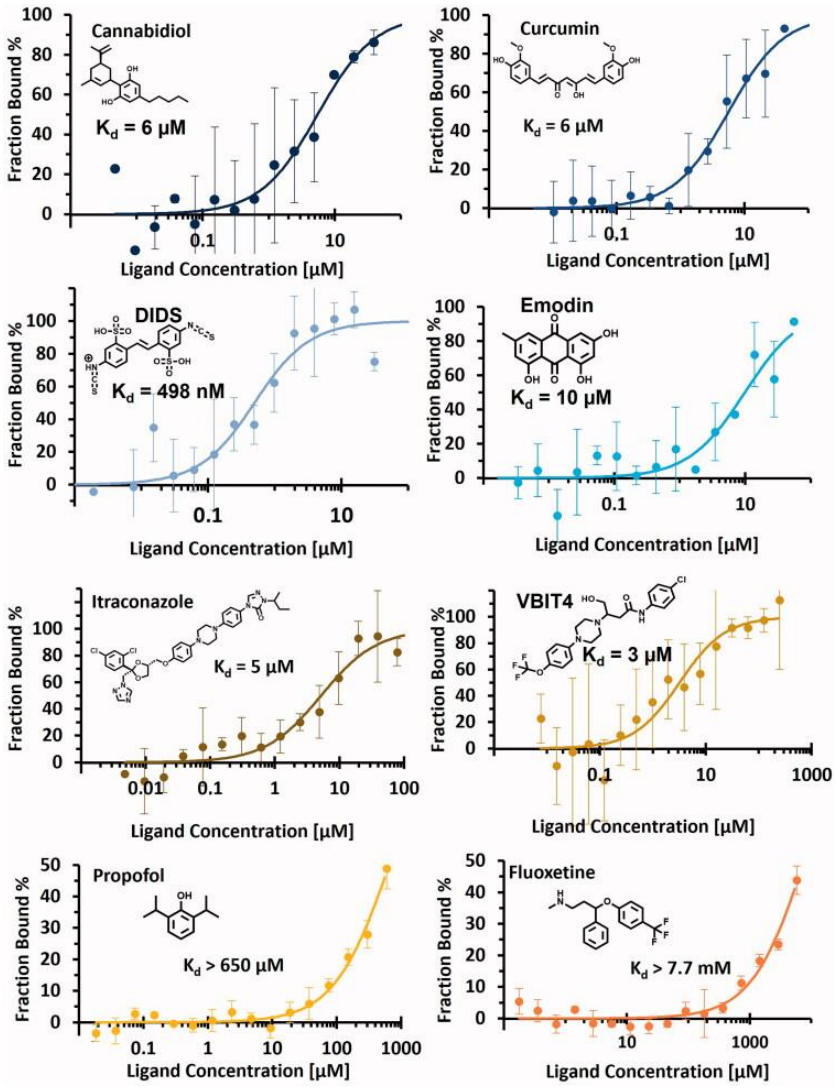

Figure 5. MST dose-response curves of eight compounds with human mitochondrial VDAC1. Precise or minimum K_D values are displayed for cannabidiol, curcumin, DIDS, emodin, itraconazole, VBIT4, propofol and fluoxetine. Error bars show standard deviation obtained from three replicas of the same measurement. This figure was reproduced from Gorny et al. (2023) [60].

In a study of competitive interactions between the phosphoinositide regulator of TRP (PIRT), the cold sensing ion channel TRPM8, and the signalling phosphoinositide lipid PIP2, MST was used identify a competitive PIRT interaction between PIP2 and the TRPM8 S1-S4 transmembrane domain [62].

MST measured binding of the tarantula gating-modifier toxins ProTx-II and GpTx-I to the voltage sensing domain (VSD) of repeat II of the human voltage-gated sodium channel NaV1.7 [63]. Residues 732-860, which contain three transmembrane helices, were recombinantly expressed, purified and reconstituted

OSF Preprint 2024 DOI: 10.31219/osf.io/pe7ut

in DMPC lipids. For MST, VSD2 in DMPC was titrated into 50 nM toxins fluorescently labelled with Alexa Fluor™ 488. Binding affinities (K_D values) for ProTx-II and GpTx-I were measured at 200 nM (160-250 nM) and 700 nM (300-1500), respectively. In comparison, IC_{50} values for ProTx-II inhibition of full-length NaV1.7 in membranes had been reported in the range 0.3-3 nM. Mutations F813A and D816A in VSD2 increased the K_D values for GpTx-I binding to 300 nM (600-3000) and 5000 nM (3000-15,000 nM), respectively [63].

In a study that demonstrated how chloride intracellular channel 1 (CLIC1) activity is not required for glioblastoma development, but its inhibition dictates glioma stem cell responsivity to novel biguanide derivatives, MST was used to measure the interaction of two biguanide compounds (Q48 and Q54) with recombinant CLIC1 protein. CLIC1 was labelled with red and blue dye kits and dose-response curves measured binding affinities of $K_D = 15.6 \pm 1.9$ μM and $K_D = 1.9 \pm 0.5$ mM for Q48 and Q54, respectively [64].

MST was used to measure direct interactions between phosphoinositides and potassium channel KcsA. Using a range of phospholipids it was found that there was a general increase in binding affinity with the number of negative charges. The phosphoinositides PI(4)P (phosphatidylinositol 4-phosphate), PI(3,4)P2 (phosphatidylinositol 3,4-bisphosphate), PI(4,5)P2 (phosphatidylinositol 4,5-bisphosphate), PI(3,4,5)P3 (phosphatidylinositol 3,4,5-trisphosphate) with two to four net negative charges produced greater binding effects than POPC (1-palmitoyl-2-oleoylphosphatidylcholine) with no charge, and POPG (1-palmitoyl-2-oleoylphosphatidylglycerol) and PI (phosphatidylinositol) with one net negative charge [65].

MST was also used to measure the direct interaction between the purified voltage-gated proton channel (Hv1) from mouse and ATP [66].

6.6. Aquaporins

MST has been used to measure interactions with some aquaporins. In a study that demonstrated how phosphorylation of human aquaporin 2 (AQP2) allosterically controls its interaction with the lysosomal trafficking regulator-interacting protein LIP5, MST was used to measure binding of fluorescently-labelled LIP5 to wild-type and mutant forms of AQP2. Non-phosphorylated wild-type AQP2 bound LIP5 with the highest affinity ($K_D = 191 \pm 43.2$ nM), whilst AQP2-ΔP242 had 20-fold lower affinity ($K_D = 3.63 \pm 0.44$ μM). AQP2-S256E ($K_D = 1.00 \pm 0.25$ μM), S261E ($K_D = 745 \pm 141$ nM), T269E ($K_D = 721 \pm 55.0$ nM), and S256E/T269E ($K_D = 652.7 \pm 62.2$ nM) all had reduced affinity. AQP2-S264E had an affinity similar to non-phosphorylated wild-type AQP2 ($K_D = 278 \pm 49.1$ nM) [67]. More recently, a protocol was developed for characterizing the binding between a human aquaporin and a soluble interaction partner using MST [68], and MST was used to measure the interaction of *Zea mays* aquaporin ZmPIP2;5 with the jasmonic acid analogue coronatine [69].

6.7. Transporters

Interactions with a variety of transport proteins have been analysed by MST, including binding of purine and pyrimidine nucleosides to equilibrative nucleoside transporter 7 (ENT7) from *Arabidopsis thaliana* fused with eGFP [70]. An MST ligand-binding assay for characterising solute carriers was demonstrated using the SLC15 oligopeptide transporter PepT1. An SLC15A1/PepT1 ortholog from the moss *Physcomitrella patens* (PepTPp), which is highly similar to human PepT1, was expressed in yeast. The method compared the analysis of solubilised total membrane preparations with or without expression of PepTPp, using a yeast strain (*Saccharomyces cerevisiae*), in which the corresponding endogenous SLC homolog is depleted and using the dipeptide glycylsarcosine (Gly-Sar) and the antiviral prodrug valacyclovir as test ligands. Gly-Sar was bound in the mM range and valacyclovir had a K_D of around 50 μM [71].

In a study that dissected the protonation sites for antibacterial recognition and transport in the multidrug efflux transporter QacA from *Staphylococcus aureus*, MST was used to measure binding of substrates to purified wild-type and mutant forms of QacA. Wild-type QacA had K_D values for binding tetraphenylphosphonium, pentamidine and dequalinium of 0.36 ± 0.07 mM, 1 ± 0.17 mM and 0.90 ± 0.21 mM, respectively [72].

In a study that identified a grafted hyaluronic acid N-acetyl-l-methionine (HA-ADH-AcMet) to target the human L-type amino acid transporter-1 (LAT1), MST was used to measure the binding affinity of different ligands to LAT1. The highest affinity ligand was HA-ADH-AcMet with a K_D of 408 nM [73].

In a study investigating functional sites in the Major Facilitator Superfamily (MFS) efflux protein NorA from *Staphylococcus aureus*, MST was used to measure the binding of tetraphenylphosphonium chloride to GFP-fused wild-type and mutant NorA. GFP was fused between residues 153 and 154 of NorA, flanked by a peptide 'GGSGG'. Tetraphenylphosphonium chloride binding to GFP-NorA and a multisite mutation (F16A/E222A/F303A/D307A) of GFP-NorA had K_D values of 7.6 ± 2 mM and 16.7 ± 6 mM, respectively [74].

OSF Preprint 2024 DOI: 10.31219/osf.io/pe7ut

Along with other techniques, MST was used in a study of the structural basis for arsenite binding and translocation of the Acr3 antiporter from *Bacillus subtilis* [75]. Acr3 is an efflux pump that confers resistance to arsenite, it has nine transmembrane helices that display a typical NhaA structure fold, with two discontinuous helices of transmembrane segments (TM4 and TM9) interacting with each other and forming an X-shaped structure. MST measured arsenite binding to GFP-labelled wild-type Acr3 and individual mutants of Acr3 (R118A, N144A, E295A, E322A) to give K_D values of 2.9, 14.8, 11.9,19.6 and 27.5 mM, respectively (Figure 6). The study identified motif C in TM9 to be a critical for substrate binding, in which N292 and E295 are involved in substrate coordination, while R118 in TM4 and E322 in TM10 are responsible for structural stabilization. Highly conserved residues on motif B in TM5 were found to be important in the protonation/deprotonation process [75].

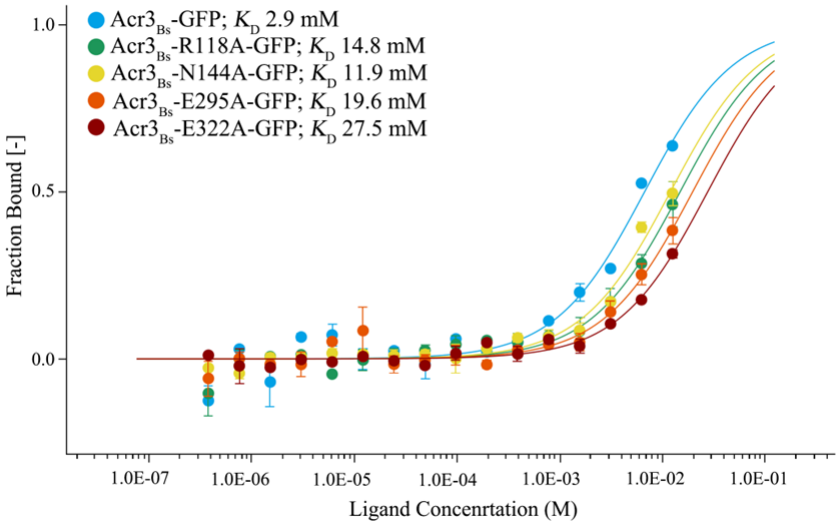

Figure 6. MST analysis of arsenite binding to GFP-labelled wild-type and mutant forms of the Acr3 antiporter from *Bacillus subtilis*. Affinity analysis with a K_D model and fitted by fraction bound normalisation. Experiments were conducted in triplicate. This figure was reproduced from Lv et al. (2022) [75].

A comprehensive study on the energy coupling and stoichiometry of Zn^{2+}/H^+ antiport by the cation diffusion facilitator YiiP from *Shewanella oneidensis* used MST to assess the binding affinity of individual Zn^{2+} binding sites and to explore the basis for coupling of Zn^{2+} transport to the proton-motive force [76]. YiiP functions as a homodimer and has three distinct Zn^{2+} binding sites referred to as A, B and C. Site A is in the transmembrane domain and has three Asp and one His residue where it is alternately exposed to the cytoplasm or to the periplasm in inward- and outward-facing states, respectively. Site B is on the loop between transmembrane helices 2 and 3 and has two His and one Asp residue. Site C is in the C-terminal domain and is a binuclear site (C1 and C2) with four His and two Asp residues. For assessing Zn^{2+} binding to individual Zn^{2+} binding sites a series of mutants was used to isolate the individual sites. The triple mutant D70A/D287A/H263A was used to study site A, D51A/D287A/H263A was used to study site B, and D51A/D70A was used to study site C. At pH 7, MST measured relatively high affinity for sites A and C with K_D values of 16 nM and 33 nM, respectively, and lower affinity for site B with a K_D value of 1.2 μM. When further mutations were introduced to isolate the individual C1 (D51A/D70A/H263A) and C2 (D51A/D70A/H234A) sites, the binding affinity was reduced to give K_D values of 153 nM and 223 nM, respectively, suggesting cooperative binding of Zn^{2+} at C1 and C2 [76]. The basis for coupling of Zn^{2+} transport to the proton-motive force was investigated by measuring Zn^{2+} binding affinities at pH values of 5.6 to 7.4.

6.8. Other membrane proteins

In a study that investigated unwinding of the substrate transmembrane helix in intramembrane proteolysis, MST measured binding of a chimeric substrate MBP-Gurken-TMD to wild-type and mutant forms of the intramembrane-cleaving proteases (I-CLiPs) rhomboid protease GlpG from *Escherichia coli* and MCMJR1 from archaea. GlpG and MCMJR1 were labelled with fluorescent dye NT-647. MBP-Gurken-TMD bound to wild-type and a mutant (H254A) of GlpG in 0.1% DDM with K_D values of ~1.4 μM and ~0.7 μM, respectively (Figure 7). Binding did not reach saturation because a higher concentration of substrate could not be achieved due to aggregation. MBP-Gurken-TMD bound to MCMJR1 in 0.1% DDM with a K_D of ~9 μM [77].

OSF Preprint 2024 DOI: 10.31219/osf.io/pe7ut

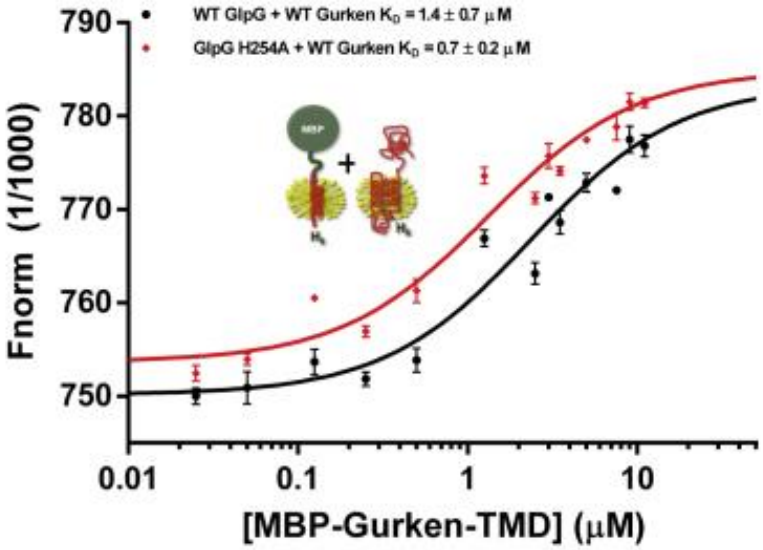

Figure 7. MST binding curves of the P252A MBP-Gurken-TMD variant to wild-type GlpG and the inactive H254A GlpG variant in 0.1% DDM. This figure was reproduced from Brown et al. (2018) [77].

In a study that demonstrated how lysosomal integral membrane protein-2 (LIMP-2/SCARB2) is involved in lysosomal cholesterol export, MST was used to detect a direct interaction between fluorescently labelled human LIMP-2 and cholesterol, giving an EC_{50} of 112 ± 32 nM [78]. In a study that demonstrated how human tetraspanin CD82 interacts with cholesterol to promote extracellular vesicle-mediated release of ezrin to inhibit tumour cell movement, MST was used to determine the cholesterol-binding affinity of CD82. MST was performed on GFP-labelled wild-type and LYK mutant CD82 proteins expressed at similar levels in Du145 cells. Cholesterol bound to CD82-wild-type with a K_D of 5.89 μM but did not bind to CD82-LYK [79].

MST was used to show how the human phosphoinositide-interacting regulator of TRP (PIRT) binds calmodulin and cholesterol-like ligands. PIRT had high affinity for calcium-free calmodulin (apo-CaM) and lower affinity for calcium bound calmodulin, with K_D values of 350 ± 40 nM and 60 ± 30 μM, respectively. Cholesteryl-hemisuccinate had a K_D of 103 ± 6 μM, and cortisol and β-estradiol had K_D values of 790 ± 60 μM and 800 ± 100 μM, respectively. Despite the structural similarity of testosterone to cholesterol, cortisol and β-estradiol, it did not show binding to PIRT [80].

Occludin is a tetramembrane-spanning tight junction protein, which possesses a bundle of three α-helices that mediates interactions with other tight junction components. A study demonstrated that serine 408 phosphorylation is a molecular switch that regulates structure and function of occludin, where a short unstructured region next to the α-helical bundle is a hotspot for phosphorylation. Here NMR was used to define the effects of S408 phosphorylation on intramolecular interactions between the unstructured region and the α-helical bundle, then paramagnetic relaxation enhancement and MST were used to demonstrate that the unstructured region interacts with the α-helical bundle, and binding was enhanced by S408 phosphorylation [81].

MST with nanodiscs was used to confirm the micromolar affinity of perforin for calcium ions, which is required for perforin interaction with the membrane. MSP nanodiscs containing 1-palmitoyl-2-oleoyl-sn-glycero-3-phosphocholine (POPC) and 1,2-dioleoyl-sn-glycero-3-phosphoethanolamine (DOPE) labelled with fluorescent dye Atto-647 (DOPEAtto-647) were used to reconstitute human and mouse perforin, giving K_D values of 123 ± 33 μM and 26 ± 5.8 μM, respectively [82].

Using multiple biophysical techniques, it was demonstrated that human mitochondrial fission protein 1 (Fis1) directly interacts with dynamin related protein 1 (Drp1) in an evolutionarily conserved manner to promote mitochondrial fission. For MST experiments, Fis1 with its N-terminal arm removed ($Fis1\Delta N^{9-125}$) and Drp1 were covalently modified at methionine residues with a Cy5-azide fluorophore. Propargyl oxaziridine was used to generate a sulfimide conjugate to methionine containing a terminal alkyne, then copper click chemistry was used to attach Cy5. In MST experiments monitoring Cys5-Drp1 fluorescence, 30 μM Drp1 was titrated with Fis1ΔN to give an apparent affinity (app K_D) of Drp1 for Fis1ΔN of 12 ± 2 μM (Figure 8) [83].

OSF Preprint 2024 DOI: 10.31219/osf.io/pe7ut

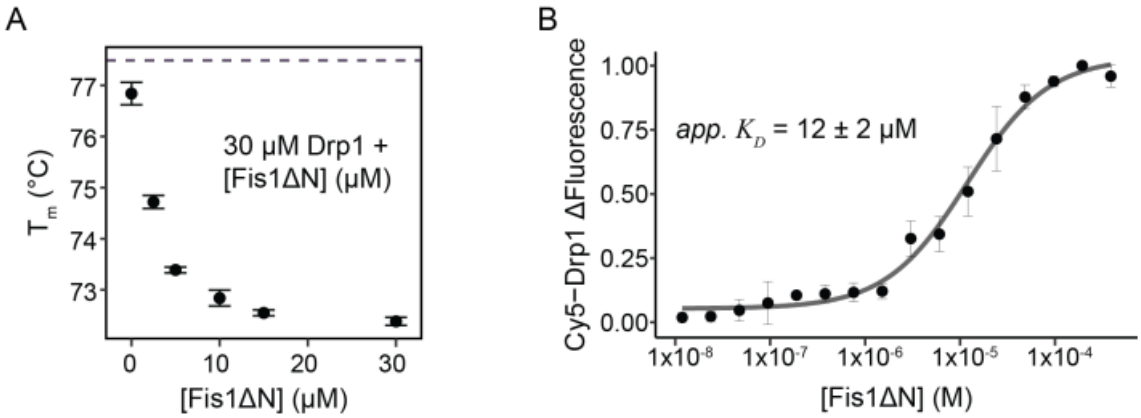

Figure 8. Removal of the Fis1 N-terminal arm reveals Drp1 binding and prevents Drp1 assembly in vitro. A. Box plot depicting the global unfolding temperature (T_m) of 30 μM Drp1 in the presence of increasing Fis1ΔN (0-30 μM). T_m values determined as the temperature corresponding to the first derivative of the maximum fluorescence value. N=2 for each titration point. B. ΔFluorescence values of 80 nM Cy5-Drp1 in the presence of increasing Fis1ΔN as determined by MST and fit to a single-site binding model to determine an apparent K_D value. ΔFluorescence values normalized to a 0-1 scale to allow for comparisons and averaging between multiple experiments (n=3), error bars=SD. This figure was reproduced from Nolden et al. (2023) [83].

7. Conclusion

In reviewing the analysis of membrane proteins by MST we have consolidated the opinion that MST is a useful technique for studying biomolecular interactions with membrane proteins. This is because MST has no limitations on the size of the target biomolecule, on the affinity of the interaction being studied or on the composition of the buffer and other sample components, and it uses much less sample compared to other techniques that measure biomolecular interactions. Different types of membrane proteins from different organisms have been studied by MST with the protein in cell lysates or native membranes, solubilised in detergents, or reconstituted in lipids, nanodiscs or Lipodisqs. Very few studies have used intrinsic aromatic residues as the fluorophore for MST measurements on membrane proteins. The large majority of studies have used membrane proteins labelled with different fluorescent dyes or conjugated with GFP. It is important that the sample conditions and the labelling strategy being used for MST measurements do not adversely affect the native structure and activity of the protein. The best studies are therefore those that use other biophysical and biochemical techniques alongside MST to test the structural integrity and activity of the membrane protein under the same conditions as those used for MST. The many interactions that MST can measure with membrane proteins include those with other proteins and peptides, nucleic acids, detergents and lipids, liposomes and vesicles, or small molecules and ions. MST is therefore a useful technique to have in drug screening projects with membrane protein targets.

Funding: This work received no external funding.

Conflicts of Interest: The authors declare no conflict of interest.

References

1. Wienken, C.J.; Baaske, P.; Rothbauer, U.; Braun, D.; Duhr, S. Protein-binding assays in biological liquids using microscale thermophoresis. *Nat. Commun.* **2010**, *1*, 100.
2. Jerabek-Willemsen, M.; Wienken, C.J.; Braun, D.; Baaske, P.; Duhr, S. Molecular interaction studies using microscale thermophoresis. *Assay Drug Dev. Technol.* **2011**, *9*, 342-53.
3. Seidel, S.A.; Dijkman, P.M.; Lea, W.A.; van den Bogaart, G.; Jerabek-Willemsen, M.; Lazic, A.; Joseph, J.S.; Srinivasan, P.; Baaske, P.; Simeonov, A.; Katritch, I.; Melo, F.A.; Ladbury, J.E.; Schreiber, G.; Watts, A. et al. Microscale thermophoresis quantifies biomolecular interactions under previously challenging conditions. *Methods* **2013**, *59*, 301-315.
4. Alexander, C.G.; Wanner, R.; Johnson, C.M.; Breitsprecher, D.; Winter, G.; Duhr, S.; Baaske, P.; Ferguson, N. Novel microscale approaches for easy, rapid determination of protein stability in academic and commercial settings. *Biochim. Biophys. Acta* **2014**, *1844*, 2241-2250.
5. Mao, Y.; Yu, L.; Yang, R.; Qu, L.B.; Harrington Pde, B. A novel method for the study of molecular interaction by using microscale thermophoresis. *Talanta* **2015**, *132*, 894-901.

OSF Preprint 2024 DOI: 10.31219/osf.io/pe7ut

6. Holdgate, G.; Embrey, K.; Milbradt, A.; Davies, G. Biophysical methods in early drug discovery. *ADMET DMPK* **2019**, *7*, 222-241.
7. Mrozowich, T.; Meier-Stephenson, V.; Patel, T.R. Microscale thermophoresis: warming up to a new biomolecular interaction technique. *Biochem. (Lond)* **2019**, *41*, 8-12.
8. El Deeb, S.; Al-Harrasi, A.; Khan, A.; Al-Broumi, M.; Al-Thani, G.; Alomairi, M.; Elumalai, P.; Sayed, R.A.; Ibrahim, A.E. Microscale thermophoresis as a powerful growing analytical technique for the investigation of biomolecular interaction and the determination of binding parameters. *Methods Appl. Fluoresc.* **2022**, *10*. doi: 10.1088/2050-6120/ac82a6.
9. Sparks, R.P.; Lawless, W.; Arango, A.S.; Tajkhorshid, E.; Fratti, R.A. Use of microscale thermophoresis to measure protein-lipid interactions. *J. Vis. Exp.* **202**2, *180*, e60607.
10. Asmari, M.; Michalcová, L.; Ibrahim, A.E.; Glatz, Z.; Wätzig, H.; El Deeb, S. Studying molecular interactions via capillary electrophoresis and microscale thermophoresis: A review. *Electrophoresis* **2023**, *44*, 1114-1142.
11. Deshayes, S.; Divita G. Fluorescence technologies for monitoring interactions between biological molecules in vitro. *Prog. Mol. Biol. Transl. Sci.* **2013**, *113*, 109-143.
12. Patching, S.G. Surface plasmon resonance spectroscopy for characterisation of membrane protein-ligand interactions and its potential for drug discovery. *Biochim. Biophys. Acta – Biomembranes* **2014**, *1838*, 43-55.
13. Siligardi, G.; Hussain, R.; Patching, S.G.; Phillips-Jones, M.K. Ligand- and drug-binding studies of membrane proteins revealed through circular dichroism spectroscopy. *Biochim. Biophys. Acta – Biomembranes* **2014**, *1838*, 34-42.
14. Patching, S.G. NMR-active nuclei for biological and biomedical applications. *Journal of Diagnostic Imaging in Therapy* **2016**, *3*, 7-48.
15. Smits, A.H.; Vermeulen, M. Characterizing protein-protein interactions using mass spectrometry: Challenges and opportunities. *Trends Biotechnol.* **2016**, *34*, 825-834.
16. Lin, K.; Wu, G. Isothermal titration calorimetry assays to measure binding affinities in vitro. *Methods Mol. Biol.* **2019**, *1893*, 257-272.
17. Vu, H.N.; Situ, A.J.; Ulmer, T.S. Isothermal titration calorimetry of membrane proteins. *Methods Mol. Biol.* **2021**, *2302*, 69-79.
18. Patching, S.G. Spermidine binding to the *Acetinobacter baumannii* efflux protein AceI observed by near-UV synchrotron radiation circular dichroism spectroscopy. *Radiation* **2022**, *2*, 228-233.
19. Niebling, S.; Burastero, O.; García-Alai, M. Biophysical characterization of membrane proteins. *Methods Mol. Biol.* **2023**, *2652*, 215-230.
20. Yang, H.C.; Li, W.; Sun, J.; Gross, M.L. Advances in mass spectrometry on membrane proteins. *Membranes (Basel)* **2023**, *13*, 457.
21. Dijkman, P.M.; Watts, A. Lipid modulation of early G protein-coupled receptor signalling events. *Biochim. Biophys. Acta.* **2015**, *1848*, 2889-2897.
22. Ormö, M.; Cubitt, A.B.; Kallio, K.; Gross, L.A.; Tsien, R.Y.; Remington, S.J. Crystal structure of the *Aequorea victoria* green fluorescent protein. *Science* **1996**, *273*, 1392-1395.
23. Remington, S.J. Green fluorescent protein: a perspective. *Protein Sci.* **2011**, *20*, 1509-1519.
24. Cormack, B.P.; Valdivia, R.H.; Falkow, S. FACS-optimized mutants of the green fluorescent protein (GFP). *Gene* **1996**, *173*, 33-38.
25. Cinelli, R.A.; Ferrari, A.; Pellegrini, V.; Tyagi, M.; Giacca, M.; Beltram, F. The enhanced green fluorescent protein as a tool for the analysis of protein dynamics and localization: local fluorescence study at the single-molecule level. *Photochem. Photobiol.* **2000**, *71*, 771-776.
26. Petruk, G.; Puthia, M.; Petrlova, J.; Samsudin, F.; Strömdahl, A.C.; Cerps, S.; Uller, L.; Kjellström, S.; Bond, P.J.; Schmidtchen, A.A. SARS-CoV-2 spike protein binds to bacterial lipopolysaccharide and boosts proinflammatory activity. *J. Mol. Cell Biol.* **2020**, *12*, 916-932.
27. Samsudin, F.; Raghuvamsi, P.; Petruk, G.; Puthia, M.; Petrlova, J.; MacAry, P.; Anand, G.S.; Bond, P.J.; Schmidtchen, A. SARS-CoV-2 spike protein as a bacterial lipopolysaccharide delivery system in an overzealous inflammatory cascade. *J. Mol. Cell Biol.* **2023**, *14*, mjac058.
28. Gawriljuk, V.O.; Zin, P.P.K.; Puhl, A.C.; Zorn, K.M.; Foil, D.H.; Lane, T.R.; Hurst, B.; Tavella, T.A.; Costa, F.T.M.; Lakshmanane, P.; Bernatchez, J.; Godoy, A.S.; Oliva, G.; Siqueira-Neto, J.L.; Madrid, P.B. et al. Machine learning models identify inhibitors of SARS-CoV-2. *J. Chem. Inf. Model.* **2021**, *61*, 4224-4235.
29. Gao, B.; Zhu, S. A fungal defensin targets the SARS-CoV-2 spike receptor-binding domain. *J. Fungi (Basel)* **2021**, *7*, 553.
30. Puhl, A.C.; Mottin, M.; Sacramento, C.Q.; Tavella, T.A.; Dias, G.G.; Fintelman-Rodrigues, N.; Temerozo, J.R.; Dias, S.S.G.; Ramos, P.R.P.D.S.; Merten, E.M.; Pearce, K.H.; Costa, F.T.M.; Premkumar, L.; Souza, T.M.L.; Andrade, C.H. et al. Computational and experimental approaches identify beta-blockers as potential SARS-CoV-2 spike inhibitors. ACS Omega **2022**, *7*, 27950-27958.
31. Song, S.; Shi Q. Interface-based design of high-affinity affibody ligands for the purification of RBD from spike proteins. *Molecules* **2023**, *28*, 6358.
32. Sadremomtaz, A.; Al-Dahmani, Z.M.; Ruiz-Moreno, A.J.; Monti, A.; Wang, C.; Azad, T.; Bell, J.C.; Doti, N.; Velasco-Velázquez, M.A.; de Jong, D.; de Jonge, J.; Smit, J.; Dömling, A.; van Goor, H.; Groves, M.R. Synthetic peptides that

OSF Preprint 2024 DOI: 10.31219/osf.io/pe7ut

antagonize the angiotensin-converting enzyme-2 (ACE-2) interaction with SARS-CoV-2 receptor binding spike protein. *J. Med. Chem.* **2022**, *65*, 2836-2847.
33. Engelhardt, P.M.; Florez-Rueda, S.; Drexelius, M.; Neudörfl, J.M.; Lauster, D.; Hackenberger, C.P.R.; Kühne, R.; Neundorf, I.; Schmalz, H.G. Synthetic α-helical peptides as potential inhibitors of the ACE2 SARS-CoV-2 interaction. *Chembiochem* **2022**, *23*, e202200372.
34. Gargantilla, M.; Francés, C.; Adhav, A.; Forcada-Nadal, A.; Martínez-Gualda, B.; Martí-Marí, O.; López-Redondo, M.L.; Melero, R.; Marco-Marín, C.; Gougeard, N.; Espinosa, C.; Rubio-Del-Campo, A.; Ruiz-Partida, R.; Hernández-Sierra, M.D.P.; Villamayor-Belinchón, L et al. C-2 thiophenyl tryptophan trimers inhibit cellular entry of SARS-CoV-2 through interaction with the viral spike (S) protein. *J. Med. Chem.* **2023**, *66*, 10432-10457.
35. Kim, S.; Liu, Y.; Lei, Z.; Dicker, J.; Cao, Y.; Zhang, X.F.; Im, W. Differential interactions between human ACE2 and spike RBD of SARS-CoV-2 variants of concern. *J. Chem. Theory Comput.* **2021**, *17*, 7972-7979.
36. Kim, S.; Liu, Y.; Ziarnik, M.; Seo, S.; Cao, Y.; Zhang, X.F.; Im, W. Binding of human ACE2 and RBD of Omicron enhanced by unique interaction patterns among SARS-CoV-2 variants of concern. *J. Comput. Chem.* **2023**, *44*, 594-601.
37. Corin, K.; Baaske, P.; Geissler, S.; Wienken, C.J.; Duhr, S.; Braun, D.; Zhang, S. Structure and function analyses of the purified GPCR human vomeronasal type 1 receptor 1. *Sci. Rep.* **2011**, *1*, 172.
38. Corin, K.; Baaske, P.; Ravel, D.B.; Song, J.; Brown, E.; Wang, X.; Wienken, C.J.; Jerabek-Willemsen, M.; Duhr, S.; Luo, Y.; Braun, D.; Zhang, S. Designer lipid-like peptides: a class of detergents for studying functional olfactory receptors using commercial cell-free systems. *PLoS One* **2011**, *6*, e25067.
39. Corin, K.; Baaske, P.; Ravel, D.B.; Song, J.; Brown, E.; Wang, X.; Geissler, S.; Wienken, C.J.; Jerabek-Willemsen, M.; Duhr, S.; Braun, D.; Zhang, S. A robust and rapid method of producing soluble, stable, and functional G-protein coupled receptors. *PLoS One* **2011**, *6*, e23036.
40. Wang, X.; Corin, K.; Baaske, P.; Wienken, C.J.; Jerabek-Willemsen, M.; Duhr, S.; Braun, D.; Zhang, S. Peptide surfactants for cell-free production of functional G protein-coupled receptors. *Proc. Natl. Acad. Sci. U. S. A.* **2011**, *108*, 9049-9054.
41. Tegler, L.T.; Corin, K.; Hillger, J.; Wassie, B.; Yu, Y.; Zhang, S. Cell-free expression, purification, and ligand-binding analysis of *Drosophila melanogaster* olfactory receptors DmOR67a, DmOR85b and DmORCO. *Sci. Rep.* **2015**, *5*, 7867.
42. Sencanski, M.; Glisic, S.; Šnajder, M.; Veljkovic, N.; Poklar Ulrih, N.; Mavri, J.; Vrecl, M. Computational design and characterization of nanobody-derived peptides that stabilize the active conformation of the β2-adrenergic receptor (β2-AR). *Sci. Rep.* **2019**, *9*, 16555.
43. Bada Juarez, J.F.; Muñoz-García, J.C.; Inácio Dos Reis, R.; Henry, A.; McMillan, D.; Kriek, M.; Wood, M.; Vandenplas, C.; Sands, Z.; Castro, L.; Taylor, R.; Watts A. Detergent-free extraction of a functional low-expressing GPCR from a human cell line. *Biochim. Biophys. Acta - Biomembranes* **2020**, *1862*, 183152.
44. Rascol, E.; Dufourquet, A.; Baccouch, R.; Soule, P.; Alves, I.D. An original approach to measure ligand/receptor binding affinity in non-purified samples. *Sci. Rep.* **2022**, *12*, 5400.
45. Wang, H.; Wang, P.; Liang, X.; Li, W.; Yang, M.; Ma, J.; Yue, W.; Fan, S. Down-regulation of endothelial protein C receptor promotes preeclampsia by affecting actin polymerization. *J. Cell. Mol. Med.* **2020**, *24*, 3370-3383.
46. Brandhofer, M.; Hoffmann, A.; Blanchet, X.; Siminkovitch, E.; Rohlfing, A.K.; El Bounkari, O.; Nestele, J.A.; Bild, A.; Kontos, C.; Hille, K.; Rohde, V.; Fröhlich, A.; Golemi, J.; Gokce, O.; Krammer, C. et al. Heterocomplexes between the atypical chemokine MIF and the CXC-motif chemokine CXCL4L1 regulate inflammation and thrombus formation. *Cell. Mol. Life Sci.* **2022**, *79*, 512.
47. Langelueddecke, C.; Roussa, E.; Fenton, R.A.; Wolff, N.A.; Lee, W.K.; Thévenod, F. Lipocalin-2 (24p3/neutrophil gelatinase-associated lipocalin (NGAL)) receptor is expressed in distal nephron and mediates protein endocytosis. *J. Biol. Chem.* **2012**, *287*, 159-169.
48. Liberelle, M.; Magnez, R.; Thuru, X.; Bencheikh, Y.; Ravez, S.; Quenon, C.; Drucbert, A.S.; Foulon, C.; Melnyk, P.; Van Seuningen, I.; Lebègue, N. MUC4-ErbB2 oncogenic complex: Binding studies using microscale thermophoresis. *Sci. Rep.* **2019**, *9*, 16678.
49. Bernhard, M.; Laube, B. Thermophoretic analysis of ligand-specific conformational states of the inhibitory glycine receptor embedded in copolymer nanodiscs. *Sci. Rep.* **2020**, *10*, 16569.
50. Li, S.Y.; Hou, L.Z.; Gao, Y.X.; Zhang, N.N.; Fan, B.; Wang, F. FIP-nha, a fungal immunomodulatory protein from *Nectria haematococca*, induces apoptosis and autophagy in human gastric cancer cells via blocking the EGFR-mediated STAT3/Akt signaling pathway. *Food Chem. (Oxf)* **2022**, *4*, 100091.
51. Saeed, M.E.M.; Yücer, R.; Dawood, M.; Hegazy, M.F.; Drif, A.; Ooko, E.; Kadioglu, O.; Seo, E.J.; Kamounah, F.S.; Titinchi, S.J.; Bachmeier, B.; Efferth, T. In silico and in vitro screening of 50 curcumin compounds as EGFR and NF-κB inhibitors. *Int. J. Mol. Sci.* **2022**, *23*, 3966.
52. Domingo, I.K.; Groenendyk, J.; Michalak, M.; Bhavsar, A.P. Cisplatin toxicity is mediated by direct binding to toll-like receptor 4 through a mechanism that is distinct from metal allergens. *Mol. Pharmacol.* **2023**, *103*, 158-165.
53. Powers, H.R.; Jenjak, S.E.; Volkman, B.F.; Sahoo, D. Development and validation of a purification system for functional full-length human SR-B1 and CD36. *J. Biol. Chem.* **2023**, *299*, 105187.
54. Gaur, P.; Seaf, M.; Trabelsi, N.; Marcu, O.; Gafarov, D.; Schueler-Furman, O.; Mandelboim, O.; Ben-Zimra, M.; Levi-Schaffer, F. 2B4 - A potential target in *Staphylococcus aureus* associated allergic inflammation. *Clin. Exp. Immunol.* **2023**, uxad089. doi: 10.1093/cei/uxad089. Epub ahead of print.

OSF Preprint 2024 DOI: 10.31219/osf.io/pe7ut

55. Hörnschemeyer, P.; Liss, V.; Heermann, R.; Jung, K.; Hunke, S. Interaction analysis of a two-component system using nanodiscs. *PLoS One* **2016**, *11*, e0149187.
56. Agnarelli, A.; Lauer Betrán, A.; Papakyriakou, A.; Vella, V.; Samuels, M.; Papanastasopoulos, P.; Giamas, C.; Mancini, E.J.; Stebbing, J.; Spencer, J.; Cilibrasi, C.; Ditsiou, A.; Giamas, G. The inhibitory properties of a novel, selective LMTK3 kinase inhibitor. *Int. J. Mol. Sci.* **2023**, *24*, 865.
57. Arbel, N.; Ben-Hail, D.; Shoshan-Barmatz, V. Mediation of the antiapoptotic activity of Bcl-xL protein upon interaction with VDAC1 protein. *J. Biol. Chem.* **2012**, *287*, 23152-23161.
58. Rimmerman, N.; Ben-Hail, D.; Porat, Z.; Juknat, A.; Kozela, E.; Daniels, M.P.; Connelly, P.S.; Leishman, E.; Bradshaw, H.B.; Shoshan-Barmatz, V.; Vogel, Z. Direct modulation of the outer mitochondrial membrane channel, voltage-dependent anion channel 1 (VDAC1) by cannabidiol: a novel mechanism for cannabinoid-induced cell death. *Cell Death Dis.* **2013**, *4*, e949.
59. Smilansky, A.; Dangoor, L.; Nakdimon, I.; Ben-Hail, D.; Mizrachi, D.; Shoshan-Barmatz, V. The voltage-dependent anion channel 1 mediates amyloid β toxicity and represents a potential target for Alzheimer disease therapy. *J. Biol. Chem.* **2015**, *290*, 30670-30683.
60. Gorny, H.; Mularoni, A.; Delcros, J.G.; Freton, C.; Preto, J.; Krimm, I. Combining nano-differential scanning fluorimetry and microscale thermophoresis to investigate VDAC1 interaction with small molecules. *J. Enzyme Inhib. Med. Chem.* **2023**, *38*, 2121821.
61. Ferens, F.G.; Patel, T.R.; Oriss, G.; Court, D.A.; Stetefeld, J. A cholesterol analog induces an oligomeric reorganization of VDAC. *Biophys. J.* **2019**, *116*, 847-859.
62. Sisco, N.J.; Helsell, C.V.M.; Van Horn, W.D. Competitive interactions between PIRT, the cold sensing ion channel TRPM8, and PIP2 suggest a mechanism for regulation. *Sci. Rep.* **2019**, *9*, 14128.
63. Schroder, R.V.; Cohen, L.S.; Wang, P.; Arizala, J.D.; Poget, S.F. Expression, purification and refolding of a human NaV1.7 voltage sensing domain with native-like toxin binding properties. *Toxins (Basel)* **2021**, *13*, 722.
64. Barbieri, F.; Bosio, A.G.; Pattarozzi, A.; Tonelli, M.; Bajetto, A.; Verduci, I.; Cianci, F.; Cannavale, G.; Palloni, L.M.G.; Francesconi, V.; Thellung, S.; Fiaschi, P.; Mazzetti, S.; Schenone, S.; Balboni, B. et al. Chloride intracellular channel 1 activity is not required for glioblastoma development but its inhibition dictates glioma stem cell responsivity to novel biguanide derivatives. *J. Exp. Clin. Cancer Res.* **2022**, *41*, 53.
65. Kiya, T.; Takeshita, K.; Kawanabe, A.; Fujiwara, Y. Intermolecular functional coupling between phosphoinositides and the potassium channel KcsA. *J. Biol. Chem.* **2022**, 298, 102257.
66. Kawanabe, A.; Takeshita, K.; Takata, M.; Fujiwara, Y. ATP modulates the activity of the voltage-gated proton channel through direct binding interaction. *J. Physiol.* **2023**, *601*, 4073-4089.
67. Roche, J.V.; Survery, S.; Kreida, S.; Nesverova, V.; Ampah-Korsah, H.; Gourdon, M.; Deen, P.M.T.; Törnroth-Horsefield, S. Phosphorylation of human aquaporin 2 (AQP2) allosterically controls its interaction with the lysosomal trafficking protein LIP5. *J. Biol. Chem.* **2017**, *292*, 14636-14648.
68. Al-Jubair, T.; Steffen, J.H.; Missel, J.W.; Kitchen, P.; Salman, M.M.; Bill, R.M.; Gourdon, P.; Törnroth-Horsefield, S. Characterization of human aquaporin protein-protein interactions using microscale thermophoresis (MST). *STAR Protoc.* **2022**, *3*, 101316.
69. He, R.; Su, H.; Wang, X.; Ren, Z.; Zhang, K.; Feng, T.; Zhang, M.; Li, Z.; Li, L.; Zhuang, J.; Gong, Z.; Zhou, Y.; Duan, L. Coronatine promotes maize water uptake by directly binding to the aquaporin ZmPIP2;5 and enhancing its activity. *J. Integr. Plant Biol.* **2023**, *65*, 703-720.
70. Girke, C.; Arutyunova, E.; Syed, M.; Traub, M.; Möhlmann, T.; Lemieux, M.J. High yield expression and purification of equilibrative nucleoside transporter 7 (ENT7) from *Arabidopsis thaliana*. *Biochim, Biophys, Acta* **2015**, *1850*, 1921-1929.
71. Clémençon, B.; Lüscher, B.P.; Hediger, M.A. Establishment of a novel microscale thermophoresis ligand-binding assay for characterization of SLC solute carriers using oligopeptide transporter PepT1 (SLC15 family) as a model system. *J. Pharmacol. Toxicol. Methods* **2018**, *92*, 67-76.
72. Majumder, P.; Khare, S.; Athreya, A.; Hussain, N.; Gulati, A.; Penmatsa, A. Dissection of protonation sites for antibacterial recognition and transport in QacA, a multi-drug efflux transporter. *J. Mol. Biol.* **2019**, *431*, 2163-2179.
73. Waddad, A.Y.; Ramharack, P.; Soliman, M.E.S.; Govender, T. Grafted hyaluronic acid N-acetyl-l-methionine for targeting of LAT1 receptor: In-silico, synthesis and microscale thermophoresis studies. *Int. J. Biol. Macromol.* **2019**, *125*, 767-777.
74. Shang, Y.; Lv, P.; Su, D.; Li, Y.; Liang, Y.; Ma, C.; Yang, C. Evolutionary conservative analysis revealed novel functional sites in the efflux pump NorA of *Staphylococcus aureus*. *J. Antimicrob. Chemother.* **2022**, *77*, 675-681.
75. Lv, P.; Shang, Y.; Zhang, Y.; Wang, W.; Liu, Y.; Su, D.; Wang, W.; Li, C.; Ma, C.; Yang, C. Structural basis for the arsenite binding and translocation of Acr3 antiporter with NhaA folding pattern. *FASEB J.* **2022**, *36*, e22659.
76. Hussein, A.; Fan, S.; Lopez-Redondo, M.; Kenney, I.; Zhang, X.; Beckstein, O.; Stokes, D.L. Energy coupling and stoichiometry of Zn^{2+}/H^{+} antiport by the cation diffusion facilitator YiiP. *eLife* **2023**, *12*, RP87167.
77. Brown, M.C.; Abdine, A.; Chavez, J.; Schaffner, A.; Torres-Arancivia, C.; Lada, B.; JiJi, R.D.; Osman, R.; Cooley, J.W.; Ubarretxena-Belandia, I. Unwinding of the substrate transmembrane helix in intramembrane proteolysis. *Biophys. J.* **2018**, *114*, 1579-1589.

OSF Preprint 2024 DOI: 10.31219/osf.io/pe7ut

78. Heybrock, S.; Kanerva, K.; Meng, Y.; Ing, C.; Liang, A.; Xiong, Z.J.; Weng, X.; Ah Kim, Y.; Collins, R.; Trimble, W.; Pomès, R.; Privé, G.G.; Annaert, W.; Schwake, M.; Heeren, J. et al. Lysosomal integral membrane protein-2 (LIMP-2/SCARB2) is involved in lysosomal cholesterol export. *Nat. Commun.* **2019**, *10*, 3521.
79. Huang, C.; Hays, F.A.; Tomasek, J.J.; Benyajati, S.; Zhang, X.A. Tetraspanin CD82 interaction with cholesterol promotes extracellular vesicle-mediated release of ezrin to inhibit tumour cell movement. *J. Extracell. Vesicles* **2019**, *9*, 1692417.
80. Sisco, N.J.; Luu, D.D.; Kim, M.; Van Horn, W.D. PIRT the TRP channel regulating protein binds calmodulin and cholesterol-like ligands. *Biomolecules* **2020**, *10*, 478.
81. Srivastava, A.K.; Venkata, B.S.; Sweat, Y.Y.; Rizzo, H.R.; Jean-François, L.; Zuo, L.; Kurgan, K.W.; Moore, P.; Shashikanth, N.; Smok, I.; Sachleben, J.R.; Turner, J.R.; Meredith, S.C. Serine 408 phosphorylation is a molecular switch that regulates structure and function of the occludin α-helical bundle. *Proc. Natl. Acad. Sci. U. S. A.* **2022**, *119*, e2204618119.
82. Naneh, O.; Kozorog, M.; Merzel, F.; Gilbert, R.; Anderluh, G. Surface plasmon resonance and microscale thermophoresis approaches for determining the affinity of perforin for calcium ions. *Front. Immunol.* **2023**, *14*, 1181020.
83. Nolden, K.A.; Harwig, M.C.; Hill, R.B. Human Fis1 directly interacts with Drp1 in an evolutionarily conserved manner to promote mitochondrial fission. *J. Biol. Chem.* **2023**, *299*, 105380.

OSF Preprint 2024 DOI: 10.31219/osf.io/pe7ut

Supplementary Material

Microscale Thermophoresis Analysis of Membrane Proteins

Nighat Nawaz[1,2], Roshan Ali[3], Muhammad Ali[3], Iain W. Manfield[4], Muhammad Kamran Taj[5], Mohammad Zahid Mustafa[5] and Simon G. Patching[1,*]

[1]School of Biomedical Sciences (Astbury Building), University of Leeds, Leeds LS2 9JT, UK
[2]Department of Chemistry, Islamia College Peshawar, Peshawar 25120, Pakistan
[3]Institute of Basic Medical Sciences, Khyber Medical University, Peshawar 25100, Pakistan
[4]School of Molecular and Cellular Biology, University of Leeds, Leeds LS2 9JT, UK
[5]Centre for Advanced Studies in Vaccinology and Biotechnology, University of Balochistan, Quetta 08763, Pakistan

*Correspondence: Professor Simon G. Patching
E-mail: s.g.patching@leeds.ac.uk, simonpatching@yahoo.co.uk

Table S1. Membrane proteins analysed by microscale thermophoresis.

Membrane protein	AA/ MW	TM domains	Sample conditions	Fluorophore	Measurements	Reference
SARS-CoV-2 spike protein						
SARS-CoV-2 spike protein (residues 16 to 1213) UniProt: P0DTC2 (spike protein)			5 µl 20 nM labelled spike protein incubated with 5 µl of increasing concentrations of LPS (250–0.007 µM) in 10 mM Tris, pH 7.4.	Spike protein labelled with Monolith labelling kit RED-NHS	Measured binding of bacterial (*E. coli*) lipopolysaccharide to the SARS-CoV-2 spike protein, giving a K_D of 46.7 ± 19.7 nM.	Petruk et al., 2020 [26]
SARS-CoV-2 spike protein RBD (residues 331 to 528) UniProt: P0DTC2 (spike protein)	198		Lumefantrine titrated (125 µM to 3.8 nM) with 5 nM spike protein RBD in HEPES 10 mM pH 7.4, NaCl 150 mM plus 5 % glycerol, 1 mM β-mercaptoethanol and 0.1 % Triton X-100.	Monolith labelling kit RED-NHS 2nd Generation	Measured binding of the antimalarial drug lumefantrine to the SARS-CoV-2 spike protein RBD with a K_D of 259 ± 78 nM.	Gawriljuk et al., 2021 [28]
SARS-CoV-2 spike protein RBD (residues 334 to 527) UniProt: P0DTC2 (spike protein)	194		0.25 µM spike protein RBD titrated with micasin and mutant forms (0.002–62.5 µM) in 5 mM sodium phosphate with 0.05% Tween 20 (pH 7.0).	Protein labelled with fluorescent dye NT−495−NHS using Monolith NT™ Protein Labeling Kit BLUE−NHS	Measured binding of the fungal defensin micasin from *Microsporum canis* to the SARS-CoV-2 spike protein RBD to give a K_D of 5.04 ± 0.96 µM.	Gao et al., 2021 [29]
SARS-CoV-2 spike protein RBD (residues 331 to 528) UniProt: P0DTC2 (spike protein)			50 nM labelled protein in 50 mM Tris, 250 mM NaCl, pH = 7 titrated with peptide at 12.5-0.00019 µM.	Protein labelled with Monolith labelling kit RED-NHS	Measured binding of six ACE2-based synthetic peptides to the SARS-CoV-2 spike protein RBD to give K_D values of 106 ± 1, 102 ± 6, 245 ± 3, 542 ± 5, 13 ± 1 and 46 ± 5 nM.	Sadremomtaz et al., 2022 [32]
SARS-CoV-2 spike protein RBD UniProt: P0DTC2	1273/ 141.2 kDa		16 sequential 1:1 dilutions of peptide in PBS + 0.05 % (v/v)	Monolith labelling kit	Measured binding affinity of α-helical peptides for the SARS-CoV-2 spike protein RBD.	Engelhardt et al., 2022 [33]

			Tween 20 as diluent, with a final volume of 10 µL, incubated with 10 µL of 10 nM labelled RBD (final conc. 5 nM).	RED-NHS 2nd Generation		
SARS-CoV-2 spike protein RBD (331–528 AA) UniProt: P0DTC2 (spike protein)	1273/ 141.2 kDa		Labelled spike RBD at 5 nM incubated with compounds, in the concentration range 250 µM to 7.629 nM in HEPES 10 mM pH 7.4, NaCl 150 mM.	Monolith labelling kit RED-NHS	Measured binding affinity of pindolol, carvedilol, carteolol, atenolol, and bisoprolol against the SARS-CoV-2 spike protein RBD.	Puhl et al., 2022 [30]
SARS-CoV-2 spike protein UniProt: P0DTC2	1273/ 141.2 kDa		SARS-CoV-2 S, S1, S2 as well as Omicron S and S1 (40 µg) were labelled and 5 µl of 20 nM labelled proteins were incubated with 5 µl of increasing concentrations of LPS or lipid A (0.007–250 µM) in 10 mM Tris at pH 7.4.	Monolith labelling kit RED-NHS	Measured binding of lipopolysaccharide and lipid A to SARS-CoV-2 spike protein variants.	Samsudin et al., 2023 [27]
SARS-CoV-2 spike protein and RBD (residues) UniProt: P0DTC2 (spike protein)			50 nM labelled protein in PBS pH 7.1, 0.05% Tween-20, 5% dimethyl sulfoxide (DMSO), incubated with compounds in 16 2-fold dilution steps from 5 mM. Also titrated with ACE2 in the absence and presence of 0.5 mM compound.	Monolith His-tag labelling kit RED	Measured binding of C-2 thiophenyl tryptophan trimers to spike protein and its RBD, also interaction with ACE2 in absence and presence of compounds.	Gargantilla et al., 2023 [34]
SARS-CoV-2 spike protein RBD (319-541 AA) UniProt: P0DTC2 (spike protein)			0.05 µM labelled RBD with ZRBD affibodies in a gradient dilution from 2.5 µmol/L in 16	Monolith His-tag labelling kit RED	Measured binding of ZRBD affibodies to SARS-CoV-2 spike protein RBD.	Song et al., 2023 [31]

			PCR tubes in 20 mmol/L PB buffer, 0.1% Tween-20, pH 7.5.			
Angiotensin-converting enzyme 2 ACE2 from *Homo sapiens* and receptor-binding domain (RBD) of the SARS-CoV-2 spike protein UniProt: Q9BYF1 (ACE2), P0DTC2 (spike protein)	805/92.5 kDa (ACE2), 1273/ 141.2 kDa (full spike protein)		Labelled ACE2 (5 nM, final conc.) mixed with RBD proteins in a serial 15-step 2-fold dilution starting from 4 µM (for WT) or 1 µM (for Omicron) in PBS buffer with 0.1 % Pluronic® F-127.	Human ACE2 labelled with Monolith labelling kit RED-NHS	Measurement of binding affinities between human ACE2 and WT and mutants of the RBD) of the SARS-CoV-2 spike protein.	Kim et al., 2021 [35] Kim et al., 2023 [36]
GPCRs						
Vomeronasal type 1 receptor 1 from *Homo sapiens* (hVN1R1) UniProt: Q7Z5H4	357/ 40.8 kDa	7 x TM helices (GPCR)	2 µM hVN1R1 solubilised in FC14 titrated with varying concentrations of myrtenal.	Native tryptophans	Measured binding of myrtenal to hVN1R1 (EC_{50} ~ 1 µM).	Corin et al., 2011a [37]
Olfactory receptors and GPCRs (12 x + 13x + 4x) from *Homo sapiens* and *Mus musculus*		7 x TM	2 µM receptor in 10% DMSO and 0.2% FC-14 in PBS.	Native tryptophans	Measured binding of olfactory receptors and GPCRs solubilised with designer lipid-like peptides to their respective ligands.	Corin et al., 2011b [38]; Corin et al., 2011c [39]; Wang et al., 2011 [40]
Neurotensin receptor 1 (NTS1) from *Homo sapiens* UniProt: P30989	418/ 46.3 kDa	7 x TM helices (GPCR)	NTS1 in fluorescently labelled MSP1D1 nanodiscs.	MSP labelled with Alexa Fluor 647 NHS ester dye	Measured binding of G-protein subunit Gαi1 to NTS1 in MSP1D1 nanodiscs formed using different lipids an in presence of different ligands.	Dijkman and Watts, 2015 [21]
β2-adrenergic receptor (β2-AR) from *Homo sapiens* UniProt: P07550	413/ 46.5 kDa	7 x TM helices (GPCR)	Used cell lysates from HEK-293 cells transiently transfected with β2-AR tagged with the GFP2.	β2-AR tagged with GFP2	Measure binding of a 17-residue nanobody-derived peptides (P3) to the β2-AR.	Sencanski et al., 2019 [42]
Dopamine receptor 1 (D1) from *Homo sapiens* UniProt: P21728	446/ 49.3 kDa	7 x TM helices (GPCR)	Cy5-labelled neurotensin (NT) with a dilution series (10–15 points) of	Cy5	Observed binding of Cy5-labelled NT to D1 Lipodisqs with a binding affinity of >300 nM.	Bada Juarez et al., 2020 [43]

			unlabelled D1 in Lipodisqs.			
Endothelial protein C receptor (EPCR) UniProt: Q9UNN8 and Protease-activated receptor 1 (PAR-1) UniProt: P25116	238/ 26.7 kDa 425/ 47.4 kDa	1 x TM helix 7 x TM helices	1 mmol/L PAR-1 protein incubated with twofold serial dilutions of EPCR protein.	Monolith labelling kit RED-NHS	Observed binding of EPCR to PAR-1.	Wang et al., 2020 [45]
Dopamine D2 receptor (D2R) in native membranes UniProt: P14416	443/ 50.6 kDa	7 x TM helices (GPCR)	Spiperone—Cy5 at a fixed concentration of 0.125 nM, D2R concentration varied from 10^{-12} to 10^{-8} M.	Fluorescent ligand spiperone—Cy5	Measured binding of spiperone—Cy5 to D2R with induced expression in mammalian plasma cell membranes, $K_D = 5.3 \pm 1.7$ nM.	Rascol et al., 2022 [44]
Chemokine receptor CXCR4 from *Homo sapiens* UniProt: P61073	352/ 39.7 kDa (CXCR4)	7 x TM helices	MST-Red-MIF was used at a fixed concentration, mixed 1:1 with serial dilutions of either CXCL4 or CXCL4L1 (final MIF concentrations: 456 nM or 312 nM, respectively). In 10 mM Tris–HCl, pH 8.0, 0.01% BSA.	Monolith labelling kit RED-NHS	Measured interaction between MST-Red-labeled MIF and platelet chemokine CXCL4L1 ($K_D = 159.8 \pm 16.8$ nM).	Brandhofer et al., 2022 [46]
Other receptors						
Lipocalin-2 (24p3/neutrophil gelatinase-associated lipocalin (NGAL)) receptor (SLC22A17) from *Homo sapiens* UniProt: Q8WUG5	538/ 57.7 kDa	11 x TM helices	Constant 24p3R-CHO membrane vesicles titrated with labelled metallothionein (20 nm-10 µm).	Metallothionein labelled with Alexa Fluor 546 fluorescent dye	Measured binding of metallothionein to 24p3R in CHO plasma membrane vesicles, giving an EC_{50} of 123 ± 50 nM.	Langelueddecke et al., 2012 [47]
Membrane-bound mucin MUC4 β-subunit from *Homo sapiens* UniProt: Q99102 (full protein) and ErbB2 receptor from *Homo sapiens* UniProt: P04626	 1255/ 137.9 kDa	1 x TM helix 1 x TM helix	Lysates of CHO cells containing the transmembrane β subunit of MUC4 (MUC4β) or a mutant containing only the EGF domains (MUC4EGF3+1+2).	GFP-labelled MUC4β Monolith His-tag labelling kit RED	Measured interactions between MUC4 β and the ErbB2 receptor.	Liberelle et al., 2019 [48]

Glycine receptor (GlyR) subunit alpha-1 from *Homo sapiens* UniProt: P23415	457/ 52.6 kDa	4 x TM helices (pentamer)	400 nM labelled α1-His GlyR in styrene-maleic acid copolymer nanodiscs in PBS added in a 1:1 ratio to a 1:2 dilution series with final concentrations of 3 mM to 0.73 µM for glycine or 12.5 mM to 6 µM for taurine.	α1-His GlyR labelled with Monolith His-tag labelling kit RED	Measured binding of full agonist glycine and partial agonist taurine to fluorescence-labelled α1-His GlyR, giving EC50 values of 65 ± 22.8 µM and 473.8 ± 66.1 µM, respectively.	Bernhard and Laube, 2020 [49]
Epidermal growth factor receptor (EGFR) from *Homo sapiens* UniProt: P00533	1210/ 134.3 kDa	1 x TM helix		Monolith labelling kit RED-NHS	Measured binding of FIP-nha (a fungal immunomodulatory protein from Nectria haematococca) to labelled EGFR (K_D = 15.54 ± 2.93 µM).	Li et al., 2022 [50]
Epidermal growth factor receptor (EGFR) from *Homo sapiens* UniProt: P00533	1210/ 134.3 kDa	1 x TM helix	200 nM EGFR with curcumin and derivatives at 100 to 100,000 nM.	Monolith labelling kit RED-NHS	Measured binding of curcumin (K_D = 5.1 ± 0.33 µM), N-(3-nitrophenylpyrazole) curcumin (K_D = 19.7 ± 2.1 µM), and curcumin derivative 1A9 (K_D = 4.9 ± 0.62 µM) to EGFR.	Saeed et al., 2022 [51]
Toll-like receptor 4 (TLR4) from *Homo sapiens* and *Mus musculus* (mouse) UniProt: O00206 (human), Q9QUK6 (mouse)	839/ 95.7 kDA (human), 835/ 95.5 kDa (mouse)	1 x TM helix	hTLR4 (100 mg/mL) or mTLR4 (100 mg/mL) in PBS containing 2% dimethylsulfoxide and 0.5% Tween-20.		Measurement of nickel and cisplatin binding to hTLR4 with K_D values of 2.72 µM and 50.57 µM, respectively. mTLR4 directly bound cisplatin (K_D = 104.9 µM) but not nickel.	Domingo et al., 2023 [52]
Natural killer cell receptor 2B4 (CD244) from *Homo sapiens* UniProt: Q9BZW8	370/ 41.6 kDa	1 x TM helix			Measured binding of Staphylococcus enterotoxin B (SEB) to 2B4.	Gaur et al., 2023 [54]
Class B scavenger receptors from *Homo sapiens* Scavenger receptor class B member 1 (SR-B1) UniProt: Q8WTV0 CD36 UniProt: P16671	 552/ 60.9 kDa 472/ 53.0 kDa	 2 x TM helices 2 x TM helices	20 nM labelled receptor incubated with a 16-step dilution series of ligand.	Monolith labelling kit RED-NHS	Measured binding of lipoprotein ligands to labelled SR-B1 and CD36.	Powers et al., 2023 [53]

Sensor kinases						
Sensor histidine kinase CpxA from *Escherichia coli* UniProt: P0AE82	457/ 51.6 kDa	2 x TM helices	CpxA-Strep reconstituted into nanodiscs at a final concentration of 300 nM. CpxR or CpxP diluted in HEPES-buffered saline creating a dilution series of 16 1:1 dilutions (735 to 0.02 µM for CpxP and 475 to 0.014 µM for CpxR).	CpxA-Strep or MSP1D1 labelled using Monolith labelling kit RED-NHS	Measured binding of CpxR (K_D = 3.7 ± 0.5 µM and 0.55 ± 0.06 µM in presence of ATP) and CpxP (K_D > 100 µM) to CpxA reconstituted in in nanodiscs.	Hörnschemeyer et al., 2016 [55]
Lemur tyrosine kinase 3 (LMTK3) from *Homo sapiens* UniProt: Q96Q04	1460/ 153.7 kDa	1 x TM helix	50 nM NHS-647-labeled LMTK3 in 50 mM Tris pH 7.4, 150 mM NaCl, 10 mM $MgCl_2$, 0.05% Tween 20, 2% DMSO mixed with serial dilutions of C36 (200 µM–0.61 nM) and C28 (200 µM–3.05 nM).	Labelling with an Alexa Fluor 647 NHS ester dye	Measurement of binding affinities between LMTK3 and inhibitors C36 and C28 to give K_D values of 1.87 ± 0.2 µM and 2.50 ± 0.4 µM, respectively.	Agnarelli et al., 2023 [56]
Ion channels						
Voltage-dependent anion channel 1 (VDAC1) from *Mus musculus*	283/ 30.8 kDa	19 x β-strands	50 nm of NT647-labelled Bcl2(Δ23) or NT647-labelled Bcl-xL(Δ21) incubated with different concentrations of VDAC1 (2 nm to 2 µm) in PBS containing 0.05% Tween 20.	Bcl2(Δ23) or Bcl-xL(Δ21) labelled with Monolith labelling kit RED-NHS	Measured binding of Bcl2(Δ23) (K_D = 0.67 µm) or Bcl-xL(Δ21) (K_D = 0.72 µm) to VDAC1.	Arbel et al., 2012 [57]
Voltage-dependent anion channel 1 (VDAC1) from *Homo sapiens* UniProt: Q9Z2L0	283/ 30.8 kDa	19 x β-strands	133 nM VDAC1 incubated with different	Monolith labelling kit BLUE-NHS	Measured binding of cannabidiol to fluorescently labelled VDAC1 (K_D = 11.2 ± 6 µM).	Rimmerman et al., 2013 [58]

			concentrations of CBD.			
Voltage-dependent anion channel 1 (VDAC1) from *Homo sapiens* UniProt: P21796	283/ 30.8 kDa	19 x β-strands	Fluorescently labelled VDAC1 (100 nM) incubated with different concentrations of Aβ (1.2–100 μm) in PBS buffer.	VDAC1 labelled with Monolith labelling kit BLUE-NHS	Measured binding of Aβ to purified and labelled VDAC1, giving a K_D of 50 μm.	Smilansky et al., 2015 [59]
Mitochondrial voltage-dependent anion channel 1 (VDAC1) from *Homo sapiens* UniProt: P21796	283/ 30.8 kDa	19-strand β-barrel	100 nM hVDAC1 in 25 mM Na_2HPO_4/NaH_2PO_4 (pH 6.5), 0.1% LDAO, 2 mM DTT.	NanoTemper Protein labelling kit RED-NHS 2nd generation (L011, NanoTemper Technologies) or labelling kit BLUE-NHS (L003)	Screening of 17 compounds for interaction with hVDAC1. Then measurement of dissociation constant for 15 compounds with 6 successfully determined.	Gorny et al., 2023 [60]
Voltage-dependent anion-selective channel (VDAC) from *Neurospora crassa* UniProt: P07144	283/ 30 kDa	β-strands	100 nM labelled VDAC incubated with hexokinase I or II in 20 mM MOPS, 100 mM NaCl, and 0.3% DM.	VDAC labelled with Alexa Fluor 647 NHS ester dye	Measured binding of hexokinase isoforms I and II to VDAC. Binding of HK-I gave a binding constant of 27 ± 6 μM in the presence of cholesteryl-hemisuccinate.	Ferens et al., 2019 [61]
Phosphoinositide-interacting regulator of TRP (PIRT) from *Homo sapiens* UniProt: P0C851 Cold sensing ion channel TRPM8 transmembrane domain S1-S4	137/ 15.3 kDa	2 x TM helices 4 x TM helices	hPIRT purified and solubilized in 0.1% DPC in 50 mM HEPES buffer at pH 7.5. 40 μL of 400 nM hPIRT was used.	hPIRT labelled with Nanotemper green maleimide reactive fluorophore	Measured competitive PIRT interaction between PIP2 and the TRPM8 S1-S4 transmembrane domain.	Sisco et al., 2019 [62]
Voltage sensing domain (VSD) of repeat II of the voltage-gated sodium channel NaV1.7 (residues 732–860) from *Homo sapiens* UniProt: Q15858	129/ 14.5 kDa	3 x TM helices	VSD2 reconstituted in DMPC lipids was titrated into 50 nM fluorescently labelled ProTx-II.	Toxins labelled with Alexa Fluor 488 fluorescent dye	Measured binding of tarantula gating-modifier toxins ProTx-II and GpTx-I to the VSD of repeat II of NaV1.7, producing K_D values of 200 nM and 700 nM, respectively.	Schroder et al., 2021 [63]

Chloride intracellular channel-1 (CLIC1) from *Homo sapiens* UniProt: O00299	241/ 26.9 kDa		10 nM or 100 nM CLIC1 for RED or BLUE labelling, respectively in 10 mM HEPES (pH 8.00), 150 mM NaCl, 0.05% Tween20. Q48 up to 5 mM and Q54 up to 15 mM.	Monolith labeling kit RED-NHS (ammine dye NT-647-NHS) and Monolith labelling kit BLUE-NHS (ammine dye NT-495-NHS)	Measured binding of two biguanide compounds (Q48 and Q54) with recombinant CLIC1 protein. $K_D = 15.6 \pm 1.9$ µM and 1.9 ± 0.5 mM, for Q48 and Q54, respectively.	Barbieri et al., 2022 [64]
Potassium channel KcsA from *Streptomyces lividans* UniProt: P0A334	160/ 17.7 kDa	2 x TM helices (tetramer)	50 nM KcsA titrated with a 1:1 dilution series of lipids over 0.25 to 0.0000153 mM in 150 mM KCl, 10 mM Hepes (pH 7.0, adjusted with NaOH), and 0.1% Tween 20.	Labelled using the Monolith His-tag labelling kit RED	Measured binding of various phospholipids to KcsA.	Kiya et al., 2022 [65]
Voltage-gated proton channel (Hv1) from *Mus musculus* UniProt: Q3U2S8	269/ 31.2 kDa	4 x TM helices			Measured the direct interaction between purified Hv1 and ATP.	Kawanabe et al., 2023 [66]
Aquaporins						
Aquaporin 2 (AQP2) from *Homo sapiens* UniProt: P41181	271/ 28.4 kDa	6 x TM helices	WT and mutant AQP2 in 20 mm Tris, pH 8, 300 mm NaCl, 0.2% OGNPG titrated with LIP5 in a 2:1 dilution series resulting in 16 different samples.	LIP5 labelled with Monolith labelling kit RED-NHS	Measured binding of labelled LIP5 to wild-type and mutant forms of AQP2.	Roche et al., 2017 [67]
Aquaporins from *Homo sapiens*			20 mM Tris pH 8.0, 300 mM NaCl, 1% OG	Alexa Fluor 488 fluorescent dye	Protocol for measuring binding of aquaporins to a soluble binding partner.	Al-Jubair et al., 2022 [68]
Aquaporin ZmPIP2;5 from *Zea mays* UniProt: Q9XF58	285/ 29.8 kDa	6 x TM helices			Interaction of ZmPIP2;5 with coronatine	He et al., 2023 [69]
Transporters						
Equilibrative nucleoside transporter 7 (ENT7) from *Arabidopsis thaliana* UniProt: Q944P0	417/ 45.7 kDa	11 x TM helices		Enhanced green fluorescent	Measured binding of purine and pyrimidine nucleosides to ENT7-eGFP.	Girke et al., 2015 [70]

				protein (eGFP)-labelled ENT7		
SLC15 oligopeptide transporter PepTPp from the moss *Physcomitrella patens* UniProt: P46059 (human)	708/ 78.8 k Da	12 x TM helices			Measured binding of the dipeptide glycylsarcosine (Gly-Sar) (mM range) and the antiviral prodrug valacyclovir (K_D ~ 50 µM) to PePTPp in total membranes.	Clémençon et al., 2018 [71]
Multidrug efflux transporter QacA from *Staphylococcus aureus* UniProt: P0A0J9	514/ 55.0 kDa	14 x TM helices	50 nM labelled QacA incubated with 16 two-fold serial dilutions of substrates in 30 mM phosphate buffer, (pH 7.0), 120 mM NaCl, 1 mM UDM, 5% glycerol.	Monolith His-tag labelling kit RED	Measured binding of substrates to purified WT and mutant forms of QacA. WT QacA had K_D values for binding tetraphenylphosphonium, pentamidine and dequalinium of 0.36 ± 0.07 mM, 1 ± 0.17 mM and 0.90 ± 0.21 mM, respectively.	Majumder et al., 2019 [72]
l-type amino acid transporter-1 (LAT1) from *Homo sapiens* UniProt: Q01650	507/ 55.0 kDa	12 x TM helices			Measured binding affinity for different ligands with LAT1, including the highest affinity ligand hyaluronic acid N-acetyl-l-methionine (HA-ADH-AcMet) with a K_D of 408 nM.	Waddad et al., 2019 [73]
Efflux pump NorA from *Staphylococcus aureus* UniProt: P0A0J7	388/ 42.3 kDa	12 x TM helices		GFP fused between residues 153 and 154 of NorA and flanked by a peptide 'GGSGG'	Measured tetraphenylphosphonium chloride binding to a multisite mutation (F16A/E222A/F303A/D307A) of NorA.	Shang et al., 2022 [74]
Acr3 antiporter from *Bacillus subtilis* UniProt: P45946	346/ 38.3 kDa	9 x TM helices		GFP-labelled	Measured arsenite binding to GFP-labelled WT Acr3 and individual mutants (R118A, N144A, E295A, E322A) to give K_D values of 2.9, 14.8, 11.9,19.6 and 27.5 mM, respectively.	Lv et al., 2022 [75]

Cation Diffusion Facilitator YiiP (Zn^{2+}/H^{+} antiporter) from *Shewanella oneidensis* UniProt: Q8E919	296/ 32.5 kDa	5 x TM helices (homodimer)	8 to 100 nM YiiP in SEC buffer (20 mM HEPES, pH 7.5,150 mM NaCl, 0.2% n-decyl-β-D-maltoside, 1 mM tris(2-carboxyethyl)phosphine).	WT and mutants of YiiP labelled with Alexa fluor 488 fluorescent dye	Measured the binding affinity of individual Zn^{2+} binding sites and explored the basis for coupling of Zn^{2+} transport to the proton-motive force. At pH 7, sites A, B and C had Kd values of 16 nM, 1.2 µM and 33 nM, respectively.	Hussein et al., 2023 [76]
Other membrane proteins						
Intramembrane-cleaving proteases (I-CLiPs) Rhomboid protease GlpG from *Escherichia coli* UniProt: P09391 and MCMJR1 from archaea	276/ 31.3 kDa	6 x TM helices	A 15-point dilution series of purified MBP-Gurken-TMD, ranging from 0.025 to 14 µM, was incubated with 14 nM GlpG or MCMJR1.	GlpG, and MCMJR1 labelled with NT-647 dye	Measured binding of MBP-Gurken-TMD to wild-type and mutant (H254A) forms of GlpG in 0.1% DDM with K_D values of ~1.4 µM and ~0.7 µM, respectively. Binding to MCMJR1 with a K_D of ~9 µM.	Brown et al., 2018 [77]
Lysosomal integral membrane protein-2 (LIMP-2/SCARB2) from *Homo sapiens* UniProt: Q14108	478/ 54.3 kDa	2 x TM helices	Labelled LIMP-2 diluted in buffer with 0.1% Fos-Choline 13 (300 mM NaAc pH 6.0, 150 mM NaCl, 0.05% Tween 20) to a concentration of 25 nM, mixed with cholesterol at 0.1 nM to 6 uM.	His-tagged LIMP-2 labelled using the Monolith His-tag labelling kit RED	Measured interaction between LIMP-2 and cholesterol with an EC50 of 112 ± 32 nM.	Heybrock et al., 2019 [78]
Tetraspanin CD82 from *Homo sapiens* UniProt: P27701	267/ 29.6 kDa	4 x TM helices	Cell lysates of Du145-eGFP-CD82 WT and -eGFP-CD82 LYK mutant transfectants used for cholesterol binding.	GFP-fused proteins	Measured cholesterol binding to GFP-labelled wild-type CD82 with a K_D of 5.89 µM, no binding to a LYK mutant.	Huang et al., 2019 [79]
Phosphoinositide-interacting regulator of TRP (PIRT) from *Homo sapiens* UniProt: P0C851	137/ 15.3 kDa	2 x TM helices	200 nM fluorescently-labelled PIRT in 0.1% DPC (w/v), 50 mM HEPES, pH 7.0 added to ligands.	Nanotemper green maleimide reactive fluorophore	Measured binding of calmodulin and cholesterol-like ligands to PIRT.	Sisco et al., 2020 [80]

Occludin from *Homo sapiens* UniProt: Q16625	522/ 59.1 kDa	4 x TM helices	Synthetic occludin 383–412 peptides with or without phosphorylation at S408 added to the recombinant occludin 413–522 α-helical bundle.	His-tagged occludin constructs labelled with a Monolith His-tag labelling kit RED	Measured binding between synthetic occludin 383–412 peptides with or without phosphorylation at S408 and the occludin 413–522 α-helical bundle.	Srivastava et al., 2022 [81]
Perforin from *Homo sapiens* UniProt: P14222 and from *Mus musculus* UniProt: P10820	555/ 61.4 kDa 554/ 62.1 kDa	2 x β-strands	16 1:1 dilutions of $CaCl_2$ in nanodisc buffer, giving concentrations of 1.53 µM to 50 mM, incubated with perforin nannodiscs	DOPE labelled with Atto-647	Measured affinity of human and mouse perforin for calcium ions, K_D = 123 ± 33 µM and 26 ± 5.8 µM, respectively.	Naneh et al., 2023 [82]
Mitochondrial fission protein 1 (Fis1) from *Homo sapiens* UniProt: Q9Y3D6	152/ 16.9 kDa	1 x TM (helical)	Cy5-Fis1ΔN$^{9-125}$ at 0-30 µM (in 20 mM HEPES, pH 7.4, 175 mM NaCl, 1 mM DTT, 0.05% TWEEN-20, 0.02% sodium azide) titrated against Cy5-Drp1 at 30 µM (in 20 mM HEPES, pH 7.4, 150 mM KCl, 2 mM $MgCl_2$, 1 mM DTT, 0.05% TWEEN-20, 0.02% sodium azide).	Cy5	Titration of Cy5-Fis1ΔN$^{9-125}$ with Cy5-Drp1 (dynamin related protein 1) to get binding affinity. app K_D 12 ± 2 µM.	Nolden et al., 2023 [83]